CO$_2$ Sorption-Desorption and Physical Properties of BaCO$_3$/CuO Composites

Maryam Tahir
NUST201463652MSNS78214F

A thesis submitted in partial fulfillment of requirements for the degree of

Master of Science in Chemistry

Supervised by

Dr. Zahida Malik

Department of Chemistry

School of Natural Sciences

National University of Sciences and Technology

Islamabad, Pakistan

2017

Dedicated to my Parents

my father for his continuous efforts in my
education and my mother for her love and prayers.

Table of Contents

List of Abbreviations

AE   Auger Electrons

Al   Aluminum

Al_2O_3 Alumina

at. %   Atomic Percentage

B   Boron

BaS   Barium Sulfide

BSE   Back Scattered Electrons

C   Carbon

Co   Cobalt

CO_2 Carbon dioxide

Cr   Chromium

Cu   Copper

CeO   Cerium Oxide

CuO   Copper Oxide

CRT   Cathode Ray Tube

CTE   Coefficient of Thermal Expansion

CCCs   Carbon/Carbon Composites

CMCs   Ceramic Matrix Composites

DRS   Diffused Reflectance Spectroscopy

DUT   Device under Test

DRIFTS Diffuse Reflectance Infrared Fourier Transform Spectroscopy

eV   Electron Volts

EDX   Energy Dispersive X-ray Spectroscopy

EMI/RFI Electromagnetic-Radiofrequency Interference Shielding

Fe   Iron

Fe_2O_3 Iron Oxide

FTIR   Fourier Transform Infrared Spectroscopy

h   Hour

ICSD   Inorganic Chemistry Structural Database

IT-SOFCs Intermediate temperature Solid Oxide Fuel Cells

JCPDS Joint Committee on Powder Diffraction Standards

K   Kelvin

kHz   kilo Hertz

LCR	Inductance, Capacitance and Resistance	TiO$_2$	Titania
LSF	Lanthanum Strontium Ferrites	V	Vanadium
Mg	Magnesium	WC	Tungsten Carbide
Mo	Molybdenum	WH	Williamson Hall
min	Minutes	XRPD	X-ray Powder Diffraction
MMCs	Metal Matrix Composites	YBCO	Yttrium Barium Copper Oxygen
N	Nitrogen	Zn	Zinc
nm	Nanometer	ZnO	Zinc Oxide
Na$_2$S	Sodium Sulfide	ZrO$_2$	Zirconia
NiO	Nickel Oxide	^{o}C	degree Celsius
NIR	Near-Infrared	$ln(F)$	Natural log of Frequency
O	Oxygen	ε	Dielectric Constant
ORR	Oxygen Reduction Reaction	ε''	Dielectric loss
PMCs	Polymer Matrix Composites	$tan\delta$	Tangent Loss
rpm	Revolutions per minute	σ_{ac}	AC conductivity
SE	Secondary Electrons	3-D	Three Dimensional
SEM	Scanning Electron Microscopy		
SiC	Silicon Carbide		
SOFCs	Solid Oxide Fuel Cells		
Ti	Titanium		
TGA	Thermogravimetric Analysis		

List of Figures

List of Tables

Acknowledgments

Abstract

A simple wet chemical route for the synthesis of barium carbonate ($BaCO_3$) has been followed by the use of atmospheric carbon dioxide (CO_2) as a carbon source while copper oxide (CuO) has been synthesized via precipitation method. Phase analysis, purity and crystallite size have been confirmed by X-ray powder diffraction (XRPD) which indicated that all the samples are in single phase with crystallite size; $BaCO_3$ = 52.4, CuO = 86.5 nm. Field emission scanning electron microscopy (FESEM) helped in determining morphology of samples, both $BaCO_3$ and CuO showed spherical geometry with average particle size; $BaCO_3$ = 200, CuO = 150 nm. Energy dispersive X-ray spectroscopy (EDX) confirmed the presence of required elements in the samples. Fourier transform infrared (FTIR) confirmed the bonding between CO_2 and barium sample by appearance of a vibration band near 1410 cm^{-1} which is due to the reaction with the surface oxygen atoms while thermogravimetric analysis (TGA) was verified the absorption of CO_2 along with the degradation temperature of $BaCO_3$ (~1400 °C). TGA results proved that sample can successfully absorb CO_2 till 1100 °C and absorbance reduces at high temperatures. $BaCO_3$ was further allowed to undergo cyclic heat treatment which showed that after 3 cycles the sample withholds CO_2 due to formation of BaO-liquid-$BaCO_3$ equilibria that arrests the further loss of CO_2. The effect of CuO on the carbonation and decarbonation of $BaCO_3$ was also studied and it was found that CuO reacts with BaO forming $BaCuO_2$ that does not allow the complete re-absorbance of CO_2.

The content of CuO controls optical and dielectric properties in $BaCO_3$/CuO composites. The band gap decreases systematically from 3.09 eV to 1.52 eV due to increased CuO contents in the composites, whereas, dielectric behavior of the composites does not show a systematic trend due to inhomogeneities (porosity, grains, defects) in the structures

which are more pronounced at high frequencies. High dielectric values (10^4 to 10^5) of the composites at low frequency (100 Hz) have been observed with low value of tangent loss. AC conductivity showed unique variation with frequency which has been explained by translational reorientational hopping.

Graphical Abstract
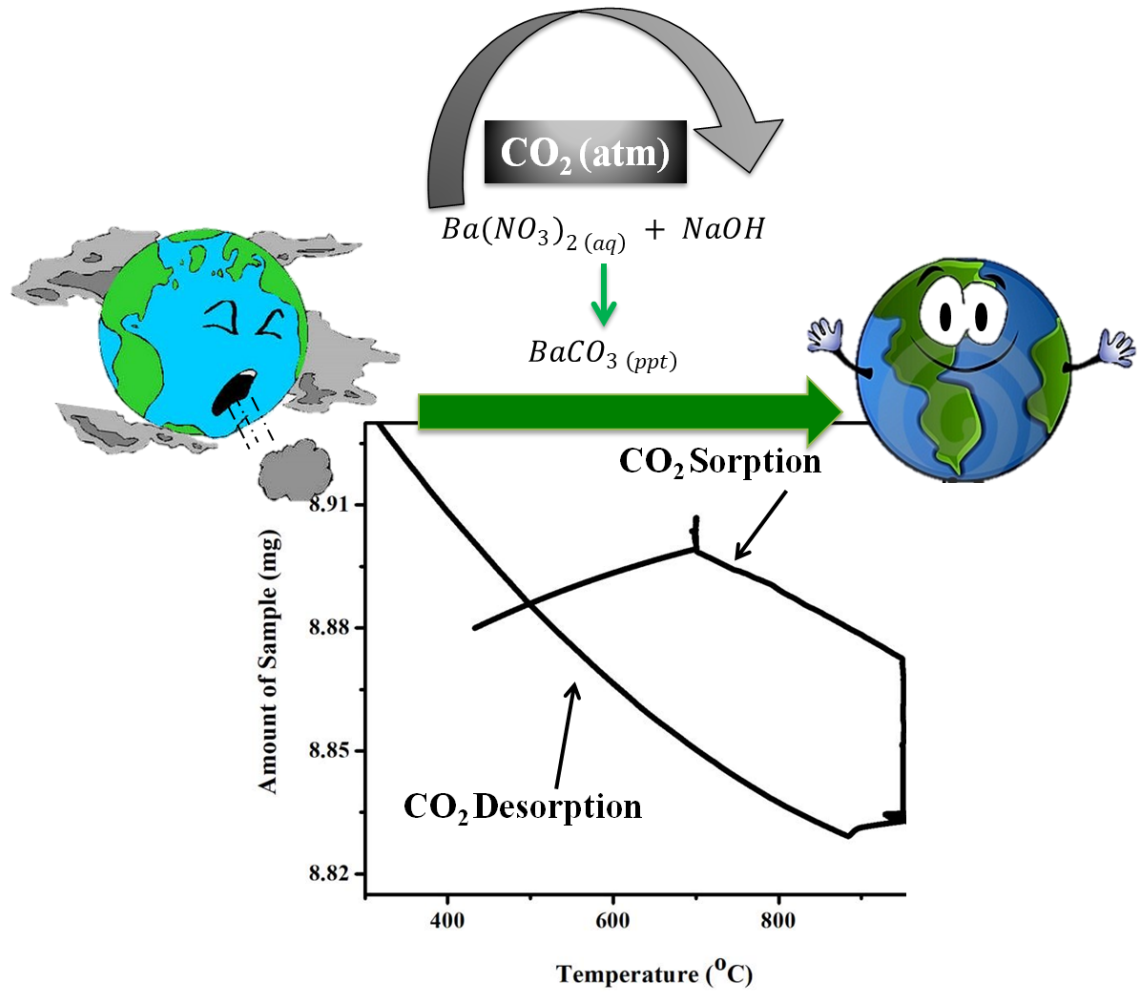
Chapter 1

Introduction

Composite materials are revolutionizing industry by replacing metals due to their low cost, high strength to weight ratio and ease of fabrication. Such versatile properties lead to applications in aerospace, energy, domestic, electrical, medical, civil construction and chemical industries.

1.1. Composites and their Types

Composition material, commonly known as composite, is a mixture of two or more chemically different and insoluble phases with unique properties, different from individual constituents. As the phases do not dissolve or blend into one another, they can be separated easily. They usually have one or more discontinuous phases, commonly known as reinforcement, embedded in a continuous phase that is matrix. On the basis of matrix material, composites can be divided into four types; Polymer Matrix Composites, Metal Matrix Composites, Ceramic Matrix Composites and Carbon/Carbon Composites [1].

1.1.1. Polymer Matrix Composites (PMCs)

PMCs consist of polymer matrix with a fibrous reinforcing dispersed phase and can be easily fabricated making them cheaper than other types of composites. They are not only light weight but also resistive to corrosion and electric current, hence useful in aeronautical applications. The polymer matrix is divided into two subgroups; thermosets and thermoplastics. Thermosets have to be post cured for further use making them rigid and unable to reform. On the other hand, thermoplastics can be softened repeatedly and

can regain the previous form on heating. New polymers with increasing temperature ability have been developed which can replace Ti in aircraft gas turbine parts [2].

1.1.2. Metal Matrix Composites (MMCs)

MMCs have metal matrix and some nonmetal/metalloid/different metal as reinforced phase. Various oxides and non-oxides ceramic materials are used as matrix in CMCs for high temperature applications [3]. MMCs can be in form of alloys e.g. Al alloys (Al-Cu-Mg, Al-Zn-Mg-Cu) Ti alloys (Ti-6%Al-4%V known as work horse), Mg alloys and Cu (niobium based superconductors) [4]. The important application of MMCs is their resistance against fire and radiation. Mg, Ti and Al have been known as popular matrix materials, useful for aircraft applications, while SiC, Al_2O_3 and B have been commonly used as reinforcement materials. The resulting composite exhibits high strength to weight ratio as compared its constituents.

1.1.3. Ceramic Matrix Composites (CMCs)

CMCs are a subcategory of composite materials, consisting of one or more metals combined with nonmetals e.g. O, N or C having strong ionic and covalent bonds. These have been designed to overcome disadvantages; low fracture/toughness, little thermal shock stability and brittleness, confronted by the traditional ceramics. The reinforcement material must be carefully chosen so that it may enhance tensile strength and other mechanical properties of ceramics rather than suppressing them. CMCs have low density and high elastic modulus. The applications utilizing temperature higher than 1100 °C require CMCs due to high stiffness and high strength at these conditions. [4].

1.1.4. Carbon/Carbon Composites (CCCs)

CCCs comprise of continuous and discontinuous carbon fiber fixed in carbon matrix. Previously, CCCs have been used because of their high temperature ablation resistance but on the expense of strength and stiffness. Later, the properties have been increased

over time and now they are being used in aircraft brakes, racing car clutches and electronic packaging. CCCs get oxidized at low temperature (~370 ^{o}C) which possesses a limit to their applications; therefore, oxidation inhibitors can be added to increase the oxidation temperature so that CCCs can maintain properties at high temperatures (~2800 ^{o}C). CCCs reinforced with ultrahigh thermal conductivity carbon fibers have been developed for thermal control applications. Moreover, the structure of CCCs is considered similar to bone and has been used for hips or joints replacement [2, 5].

1.2. Characterization Techniques

1.2.1. X-Ray Powder Diffraction (XRPD)

XRPD is a swift analytical technique mainly used for purity and phase identification of a crystalline material. It provides information on unit cell dimensions, crystal system and crystallite size by measuring the intensities and angles of the beam diffracted by the sample. In 1912, Max von Laue discovered the X-ray diffraction phenomenon. The basic principle behind XRPD is constructive interference between the crystalline sample and the monochromatic X-rays. The leading effect during this phenomenon is the scattering of X-rays which is known as diffraction. The diffraction of X-rays by the crystal has been explained by Bragg's law which states that when an X-ray interacts with the crystal it is reflected from two points, surface of the substance and atomic planes inside the substance. The distance travelled by the X-ray, reflecting from the atomic planes, depends upon the angle (θ) at which it enters the material and the separation between the atomic planes (d). For constructive interference the two reflected X-rays must have travelled an integral multiple of the wavelength (nλ). Figure 1.1 demonstrates Bragg's law.

$$n\lambda = 2dsin\theta$$
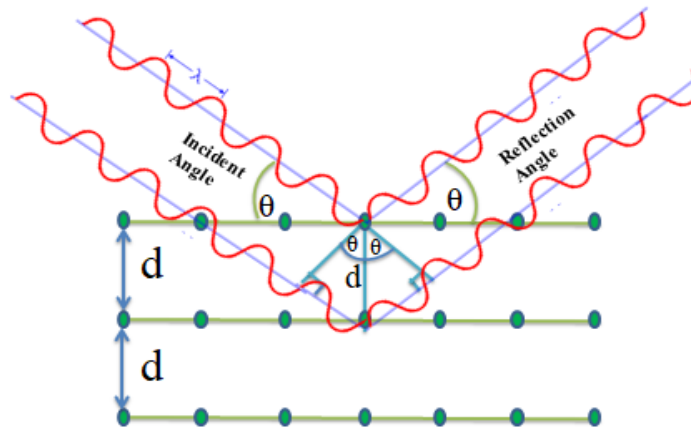
Figure 1.1: Illustration of Bragg's law.

The intensity of the diffracted waves depends on the arrangement of atoms while the angle depends upon the shape and size of the unit cell of the substance. Most of the materials do not consist of single crystals rather they have polycrystalline powder with randomly oriented crystallites. The X-ray beam analyzes all the possible interatomic planes at different angles thereby detecting all the diffraction peaks.

- ***Construction and Working of XRPD***

X-ray diffractometer consists of three basic parts; cathode ray tube (CRT), sample holder and a detector. In CRT, the filament is heated to produce electrons which are accelerated by applied voltage followed by bombardment on the target material (Cr, Fe, Co, Cu, Mo etc.). If the energy of the electrons is sufficient to emit the inner shell electrons then characteristic X-rays can be produced with wide spectra of wavelength. A monochromator is used to filter the polychromatic X-rays which are then collimated and directed onto the material. The sample holder and the detector can be rotated and intensities of the reflected X-rays are recorded. The sample rotates at an angle θ, while the detector reads the intensity of the X-ray at 2θ away from the source path. Thus the incident angle can be increased over time. *Goniometer* is used to maintain the angle and

to rotate the sample. Once the diffracted beam reaches the detector, it is processed as count rate in the software. The obtained results are then compared with the reference database in JCPDS and the crystallographic data can be determined. Figure 1.2 shows schematic diagram of XRPD [6].
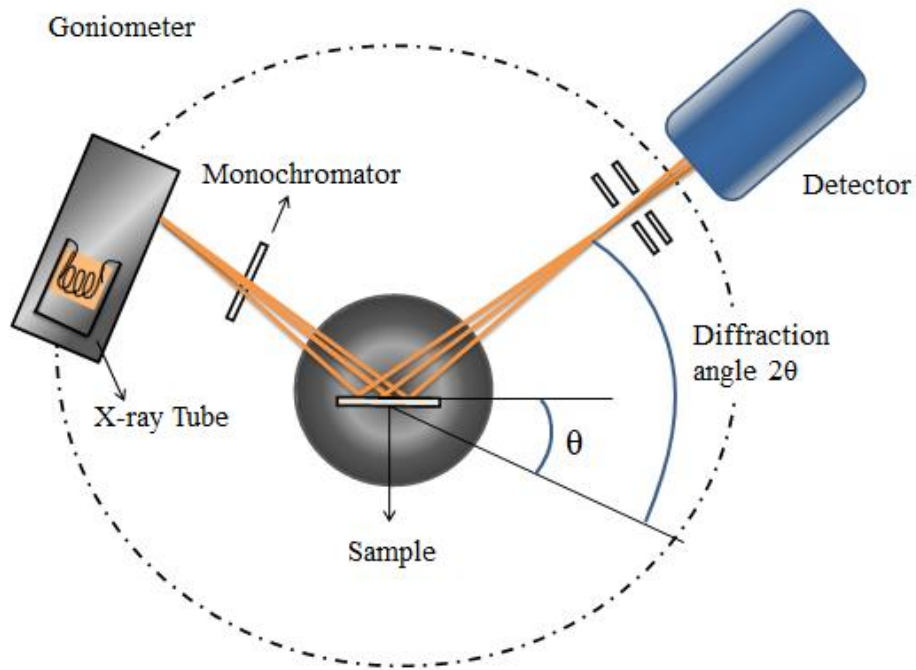
Figure 1.2: Schematic diagram of X-ray Powder Diffraction.

- *Uses and Applications of XRPD*

XRPD is a non-destructive technique which efficiently determines the crystal structure, crystallite size, phases present in the sample, atomic arrangement, lattice parameters and many other properties of the material. It is used in almost all the fields due to its versatility and accuracy in giving maximum structural information about the sample [7].

1.2.2. Scanning Electron Microscope (SEM)

The scanning electron microscope was invented by Manfred von Ardenne in 1938. A SEM uses a beam of high energy electron to form a 3-D image of the material under investigation with a resolution down to 1 nm. As it consists of electromagnets, one can control the degree of magnification. In order to be analyzed by a SEM, the object has to be conducting while for non-conducting samples, coating is done with a thin layer of gold, graphite or aluminum.

- *Construction and Working of SEM*

The essential components of SEM include; electron gun, electromagnetic lenses, object chamber, secondary electron detector and display unit. The electron gun consists of a tungsten filament which emits a stream of monochromatic electrons upon heating which are focused by the electromagnetic lenses. The first condenser lens condenses the electrons to form a beam and limits the amount of current which determines the diameter of the beam. The second condenser lens focuses the electrons into a coherent, thin beam and high angle electrons are eliminated from it by an objective aperture. The scan coils scan the beam in a grid fashion and lastly the objective lens focuses the beam on the sample. The conducting sample is placed on the sample holder which can be inserted into the high vacuum chamber. The holder can be moved along X and Y direction, in addition it can be tilted, rotated and moved in Z direction for better resolution and specific area analysis. At the rear of the sample holder, secondary electron detector is located. The velocity and angle of the secondary electrons is related to the surface structure of the material. When these electrons reach the detector, an electronic signal is produced that is amplified and transformed into a digital signal observed on the display unit for further processing. Figure 1.3 shows different components of SEM [8].
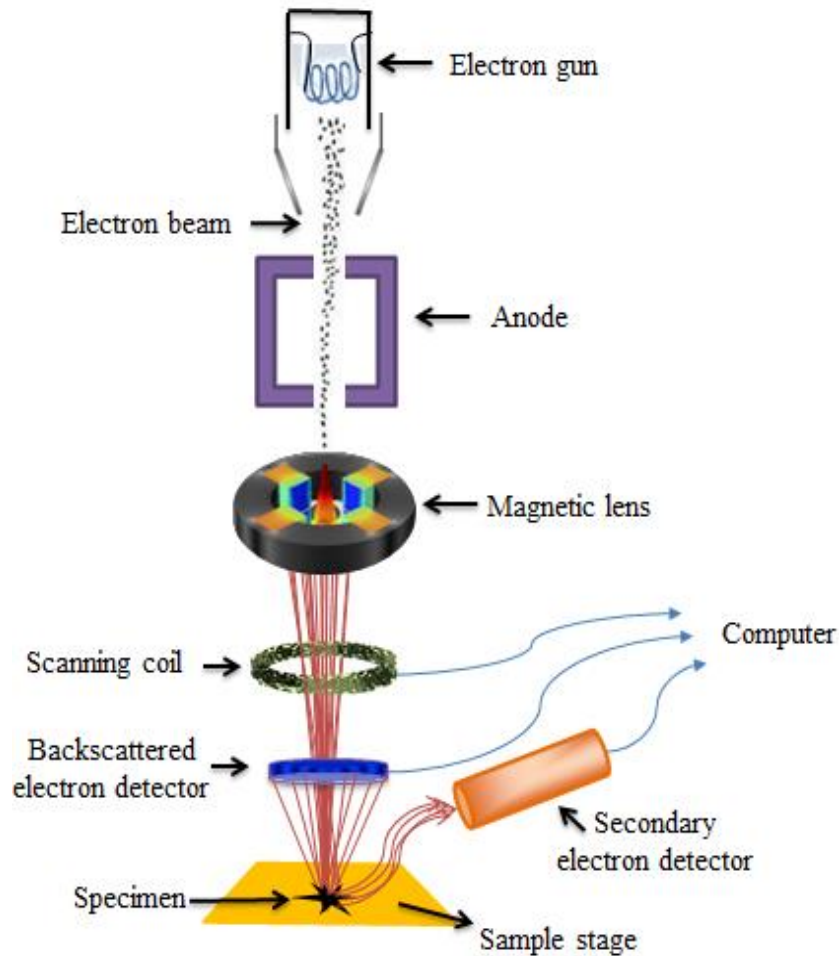
Figure 1.3: Schematic diagram of SEM.

The interaction of electron beam with the sample results in the emission of various signals which include back scattered electrons (BSE), secondary electrons (SE), auger electrons (AE) and characteristic X-rays (figure 1.4). All these signals yield different information about the sample under investigation. BSE and SE are commonly used for imaging. SE are important for evaluating the morphology and topography on samples while BSE are important for phase discrimination and are more sensitive to heavier elements than SE. AE are specifically used for surface analysis in auger electron

spectroscopy while the characteristic X-rays are used in energy dispersive X-ray spectroscopy (EDX) for elemental and compositional analysis of the sample [9].

Electron beam

Auger Electrons (AE)
Surface atomic composition

Secondary Electrons (SE)
Topographical information

Characteristic X-ray (EDX)
Thickness atomic composition

Backscattered Electrons (BSE)
Atomic number and phase difference

Fluorescent X-ray

Continuum X-ray
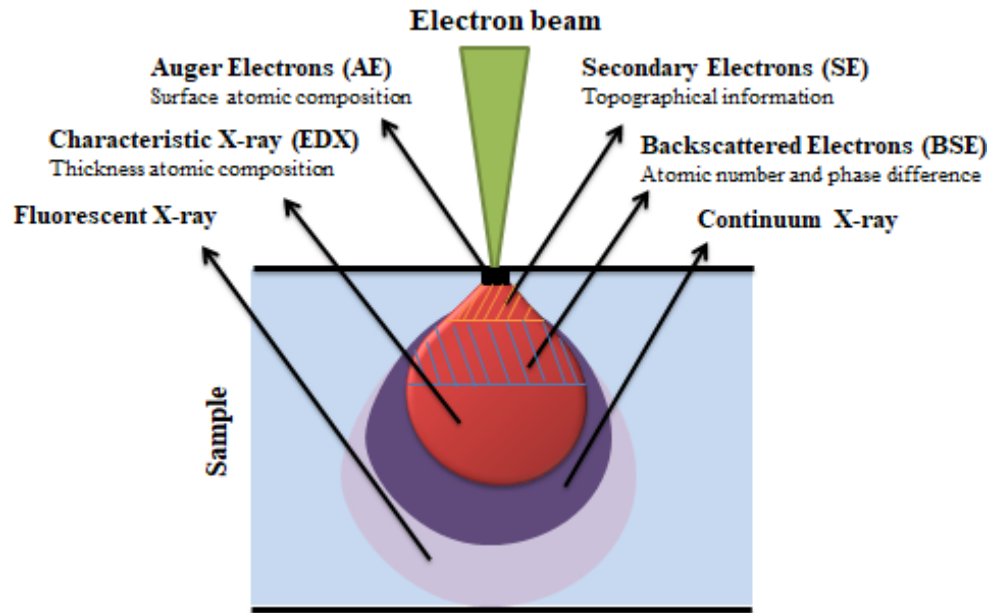
Sample

Figure 1.4: Emission of different radiations by the interaction of electron beam with the sample.

- ***Uses and Applications of SEM***

SEM is a non-destructive technique, so the same material can be analyzed repeatedly. It can be used in almost all the fields for observing structures up to 1 nm, mainly used for the topographic details of the object. BSE produced in SEM are used for phase discrimination of sample. SEM equipped with EDS can be used to find the elemental composition of the sample along with electron mapping at specific points.

1.2.3. Fourier Transform Infrared Spectroscopy (FT-IR)

Infrared spectroscopy has been a mainstay procedure for analysis of materials. An infrared spectrum is a fingerprint of a sample with absorption peaks corresponding to the

frequency of vibrations between the atomic bonds of a material. As the materials have unique combination of atoms, the infrared spectrum of every compound is different. Thus, infrared spectroscopy is a good technique for qualitative as well as quantitative analysis of every kind of material. FT-IR was developed to overcome the limitations of dispersive instruments and also to measure all the infrared frequencies simultaneously.

- *Construction and Working of FT-IR*

A normal instrument consists of a source, interferometer, sample, detector and a computer (figure 1.5). Infrared radiations are emitted from a black-body source and pass through an aperture that controls the amount of energy to be sent to the interferometer. Mostly the interferometer consists of a beam splitter which splits the infrared beam into two optical beams. One beam reflects off a flat fixed mirror while the other reflects off a flat movable mirror in such a way that both beams recombine at the beam splitter. The resulting signal is due to the interference of two beams and is called interferogram which has information about every infrared frequency coming from the source. After exiting the interferometer, the beam enters into the sample compartment where it is reflected or transmitted off of the sample surface. This is the point where the sample absorbs specific energy frequencies that are unique to it. The final measurements are carried out when the beam enters the detector which is specially designed for interferogram signal. The measured interferogram signal cannot be interpreted directly for which the individual frequencies have to be decoded. This can be accomplished by a mathematical technique called the Fourier transformation, performed by a computer. The final infrared spectrum, displayed on the screen, can be used for further interpreting and processing data [10].
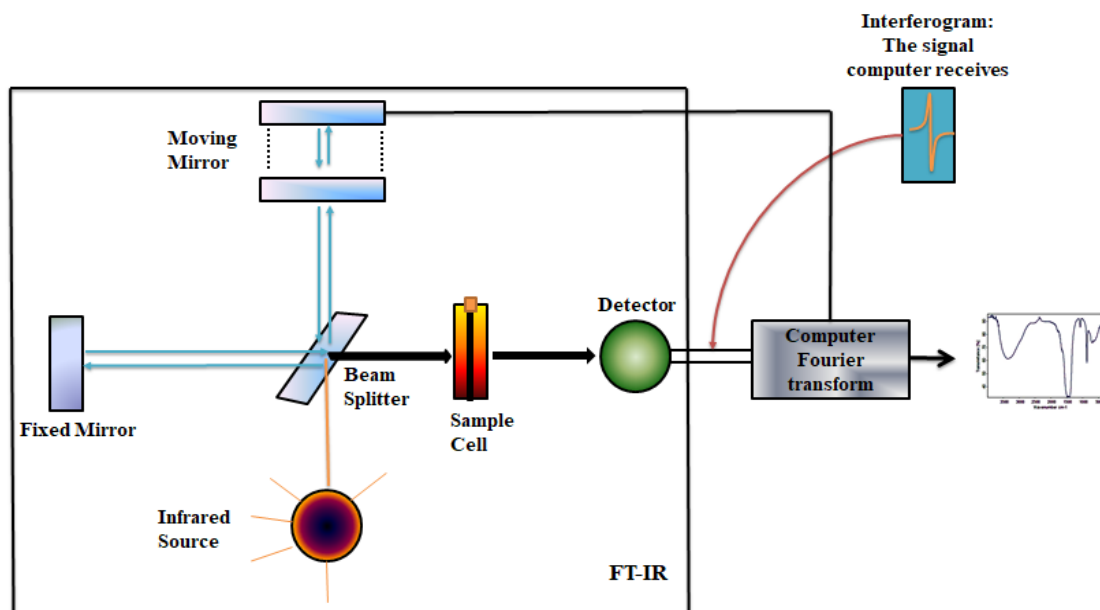
Figure 1.5: Schematic illustration of a simple FT-IR.

- ***Uses and Applications of FT-IR***

FT-IR is a reliable technique with high speed, accuracy and sensitivity to even smallest of contaminants. It is a valuable tool for quality control and has a wide variety of software algorithms making it useful for quantitative analysis.

1.2.4. UV-Vis Diffused Reflectance Spectroscopy (UV-DRS)

Diffuse reflectance is an optical phenomenon commonly used in UV-visible and infrared (near IR; NIR, mid IR; DRIFTS) regions to obtain molecular spectroscopic data. It is commonly used to obtain spectra of powdered sample and requires minimum sample preparation. A reflectance spectrum is obtained by the analysis of surface reflected electromagnetic radiations which are collected as a function of frequency (wavenumbers cm^{-1}) or wavelength (nm). Two different types of reflections can be observed, specular or regular reflection and diffuse reflection. The specular reflection is associated with the reflection from polished or smooth surfaces like mirrors while diffuse reflection is

associated with reflection from dull or rough surfaces like powders. In diffuse reflectance, the incident radiation is reflected by the sample at angles independent of the angle of incident radiation. After the interaction of the radiation with the sample, a combination of reflection, diffraction, refraction and absorption of incident radiation takes place (figure 1.6) [11].
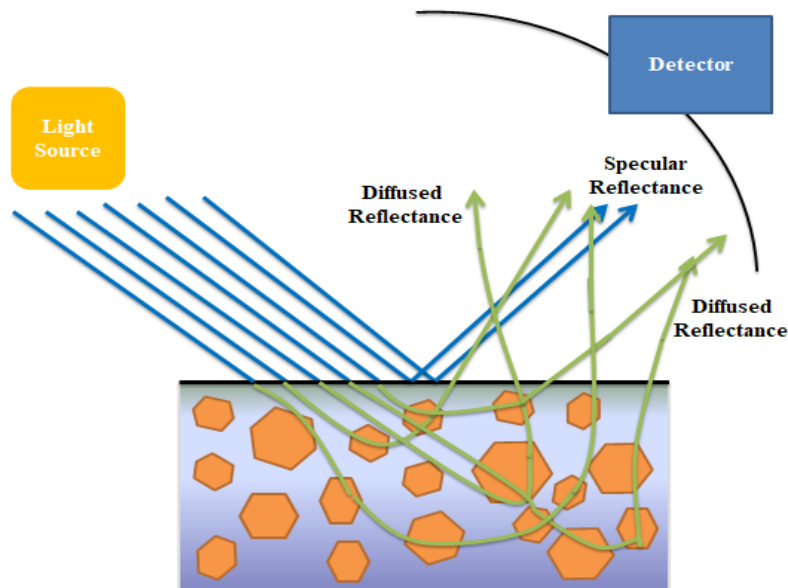
Figure 1.6: Pictorial representation of UV-DRS principle.

These phenomena are explained by different theories but the commonly used theory to describe the diffuse reflectance spectra is the Kubelka-Munk theory which is given as:

$$F(R) = \frac{(1 - R)^2}{2R}$$

Where F(R) is the Kulbelka-Munk function similar to extinction coefficient α and R is the reflectance. The band gap of the material can be obtained by multiplying the coefficient with the energy (eV):

$$E_g \ = \ [F(R) \times h\nu]^n$$

Where exponent *n* is 0.5 in case of indirect bandgap transitions and 2 in case of direct band gap transitions [12].

- ***Construction and Working of DRS***

Diffuse reflectance measurements are made using a UV-Vis spectrophotometer equipped with an integrating sphere, capable of collecting reflected flux, instead of a cell holder for transmission measurements (figure 1.7). An integrating sphere is basically a hollow sphere coated with a material (white) having diffuse reflectance near to 1 commonly Barium Sulfate ($BaSO_4$) or highly diffusing polytetrafluoroethylene (PTFE) is used as a coating agent. The integrating sphere has apertures through which the radiation passes and falls on the samples. The sample is placed in front of the incident light window and the reflected light from the sample is concentrated on the detector using an integrating sphere. So the value obtained in this case becomes relative reflectance. If the light is directed at an angle 0° on the sample, specular reflection occurs and it is not detected as a result only the diffused reflectance is measured. Thus with different models of integrating spheres, specular as well as diffused reflectance can be measured. Once the light reaches the detector, the data is analyzed via computer for further processing [11].
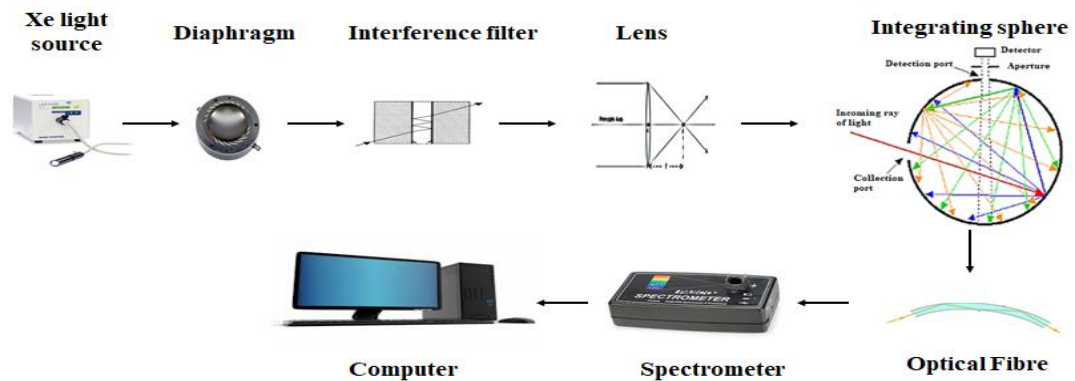
Figure 1.7: Instrumentation of a UV-DRS spectrometer.

- *Uses and Applications of DRS*

It is primarily used to calculate the band gap of materials. It is utilized in quality control of products in factories and is a refined tool for characterizing catalytic surfaces. The efficiency of solar cells can be determined by quantifying the amount of reflected light flux.

1.2.5. LCR Meter

LCR meter is named so because it can measure Inductance (L), Capacitance (C) and Resistance (R) of electronic devices. Inductance is a corresponding change in the voltage or the conductor surroundings when there is a change in the current flowing through a conductor. Capacitance is the ability of a material to store electrical charge while the opposition to the current flow or electrical charge is known as resistance.

- *Construction and Working of LCR meter*

There are two common techniques used for LCR meters; Wheatstone bridge method and current voltage measurement. The bridge method can be employed for measuring lower frequencies up to 100 kHz. A balanced bridge is used in this method so that at the balance point the bridge components can determine the value of component under test. Commonly Wheatstone bridge configuration is used in which the device under test (DUT) is placed in a bridge circuit (figure 1.8). The impedance of DUT is denoted by Z_U in the circuit while the impedance of Z_1 is variable until no current flows through Z_U whereas, the impedances of Z_2 and Z_3 are known. The oscillator circuit operates at frequencies that can be selected before the test and it normally lowers down up to 100 kHz. This is the balance position of the bridge i.e. all the four impedances obey the equation:

$$\frac{Z_U}{Z_1} = \frac{Z_3}{Z_2}$$

Hence the impedance of DUT can be determined by using equation:

$$Z_U = \frac{Z_3}{Z_2} Z_1$$
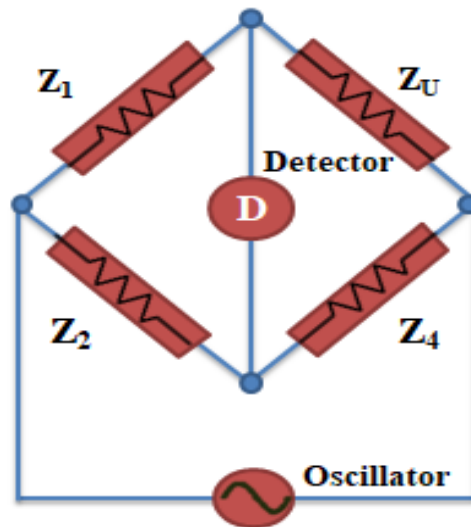
Figure 1.8: Circuit diagram for Wheatstone bridge method.

The other technique is Current-Voltage measurement which is used for higher frequency applications. It is a precise measurement technique which can be operated at wide range of frequencies. In this technique, the current and voltage are measured for which two types of voltmeter and ammeter arrangements are used; one is for low impedance while the other is for high impedance (figure 1.9). A phase sensitive detector is used to make these measurements and the relative phase of current and voltage can be used to find out the impedance of DUT in terms of inductance, capacitance and resistance. These values are separately displayed on the screen. Sometimes, a transformer is used to isolate and enable these measurement but it limits the frequency range over which the measurements are made [13], [14].
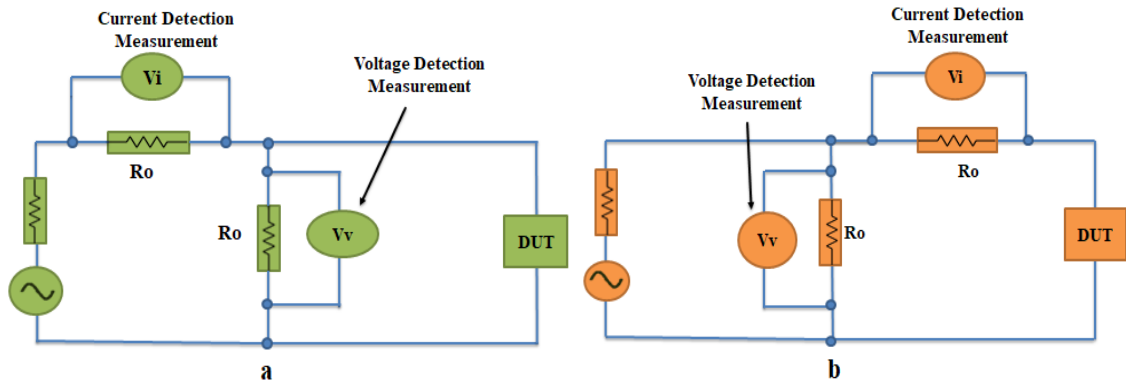
Figure 1.9: Circuit diagrams for LCR measurements at; (a) low and (b) high impedance.

- *Uses and Applications of LCR meter*

LCR meter is used for fault finding in electrical devices. It can be used to find quality factor, dissipation factor, tan loss (tanδ), and dielectric properties of the material.

1.2.6. Thermogravimetric Analysis

Thermogravimetry is an oldest thermal analytical technique and is still used for studying the thermal behavior of materials. In thermogravimetric analysis (TGA), changes in weight of a sample can be measured as a function of temperature and time. A small amount of the desired material is required for analysis and the results are obtained in the form of a TG curve with steps, depressions or hills at certain areas, describing the mass variation with temperature.

- *Construction and Working of TGA*

A TGA consists of a pan supported by a precision balance, furnace programmed for a linear change in temperature with respect to time and an inlet for gases. The sample pan used in TGA depends upon the temperature conditions; commonly used pans include alumina crucible or platinum pans. TGA requires very small amount of sample (in mg) which is placed inside the pan, adjusted on a thermobalance inside the furnace, and can

be heated or cooled at a constant heating rate during the experiment. The experiment can be carried out in air, inert gases (N_2, He, Ar), CO_2 or O_2 atmosphere depending upon reaction conditions. After inserting some desired gas, it exits through an exhaust. The mass of the sample is regularly monitored during the experiment. The mass loss indicates degradation of the sample or removal gases and moisture from the sample which appears as a step in the TG curve and if the mass is increased, it is attributed to oxidation or reaction with the surrounding substances if any indicated by a hill in the curve. Figure 1.10 illustrates instrumentation of a simple TG [15], [16].
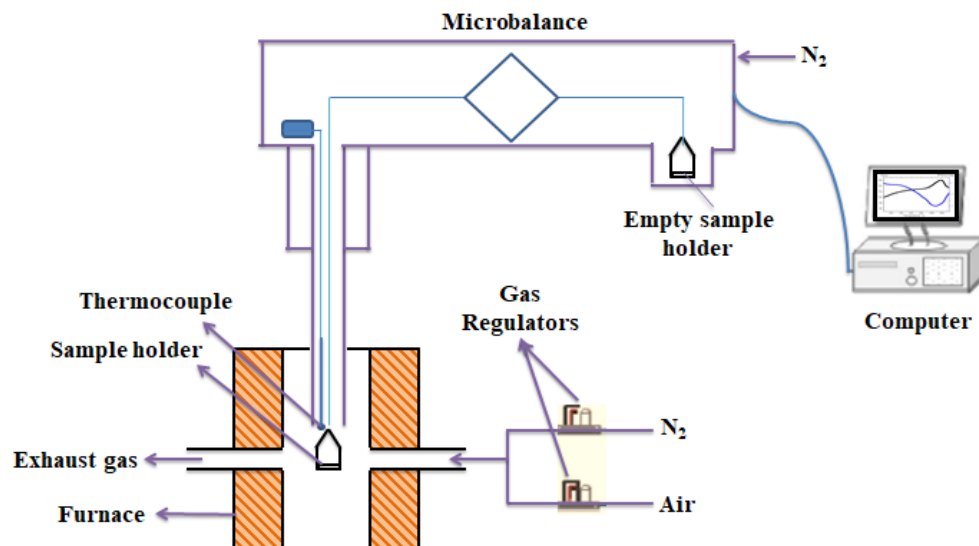
Figure 1.10: Instrumentation of a simple TG.

- *Uses and Applications of TGA*

TGA has wide applications in determining the thermal behavior, thermal stability and quality of the material. The purity of the sample, gas adsorption and desorption can be observed by this technique.

1.3.   Properties of Composites

The designing, processing and applications of composites require adequate knowledge about properties which may vary with concentration, shape, kind and properties of the constituents [17].

1.3.1.   Mechanical Properties

In early 1960s, mechanical properties studies refined the importance of composite materials. The incorporation of high strength fibers in the composites greatly improves the tensile strength, temperature resistance and flexural modulus of the resulting material, therefore, fiber must be carefully selected. MMCs reinforced with continuous fiber exhibit better mechanical behavior than PMCs due to increased transverse strength. Particle reinforcement also demonstrates good mechanical properties e.g. WC embedded in Co matrix have been used in cutting tools and dies while WC reinforced with silver is a key contact pad material in circuit breakers. CMCs have been characterized by high stiffness, resistance to oxidation and corrosion but have poor resistance to mechanical shock. To overcome this deficiency, fibers, particles and whiskers have been used as reinforcement which effectively increase the fracture toughness and ultimately the use in high strength applications [2].

Composites have high strength to weight ratio. Strong materials are often heavy as steel while some can be light as bamboo poles. The need of a single material that exhibits both properties was fulfilled by composites due to their light weight coupled with high strength. A composite can be made to resist bending in one direction while for a metal to do so; more layers of metal have to be added to gain strength at the expense of weight. Therefore, composites engineering is carried out for better strength to weight ratio. The light weight property of composites makes them suitable for vast applications where weight has to be reduced for better efficiency. Modern aircrafts such as Boeing 787 and

Dreamliner includes more composites (50% by weight) than metal body for better weight reduction[18].

1.3.2. Part Consolidation and Stability

A single piece manufactured by composites can replace a complete assembly of metal parts. The composites can be easily fabricated for construction of complicated structures. This ability of composites is useful in reducing the number of parts in a machine and saves the maintenance time and cost. Another promising property of composites is the ability to retain size and shape under severe temperature fluctuation, draught and moist conditions. On the other hand, natural composites like wood normally swell and shrink with humidity variation. Therefore, composites have been used in aircraft wings because there is a need of dimension stability at higher altitudes and variable temperatures [5], [19].

1.3.3. Thermal Properties

A possible control over thermal conductivity and thermal expansion (CTE), by regulating composition and reaction conditions lead to the multifunctional applications of composites. The CTE knowledge of material is a prerequisite while calculating dimensional changes and internal stress buildup upon exposure to temperature gradient. Thermal conductivity strongly depends on the corresponding properties of matrix and reinforcement. CCCs have been reported to show high thermal conductivities (5 times that of Cu) and can be excellent for electronic packaging applications to dispel the heat generated by the device. Particulate composites, comprising of heat conducting fillers and polymer matrix, have been used for this purpose because in addition to high thermal conductivity, they preserve the electrical insulation ability of the composites. Recently nanoparticles (Cu nanoparticles and carbon nanotubes) have been added to increase the thermal conductivity of composites [17].

1.3.4. Electrical Properties

- *Dielectric Properties*

For composites, dielectric properties are important because their dielectric response is different from that of individual components and vary with the fraction of filler content and fiber orientation. An ideal dielectric material must have high dielectric constant (high k), low dielectric loss, high breakdown strength and ease of processing. Polymers exhibit the mentioned characteristics but their dielectric constant is very low (2-5) while some materials have high dielectric constant but their dielectric loss is also high which limits their application e.g. $BaTiO_3$ has dielectric constant value in hundreds to thousands range but its high loss value makes it less useful. Therefore, to harness the advantages of polymers and ceramics, high k materials have been developed using various techniques one of which is core-shell strategy. The strategy focuses on the formation of composite by *in situ* polymerization on the nanoparticle surface resulting into PMCs with high k and low dielectric loss. High k materials have been used in energy storage devices such as capacitors. Solid $CaCu_3Ti_4O_{12}$ (CCTO) ceramics have been developed as a supercapacitor due to high dielectric constant (10^4 - 10^5 at room temperature) that is stable over a wide temperature range. Semiconducting grains and insulating grain boundaries make a heterogeneous structure which leads to high dielectric values. Doping of materials that can enhance the boundary resistance is another important technique to reduce the dielectric loss; hence composites can be designed and fabricated according to the need and application [20]–[22].

- *Optical Properties*

Optical properties of carbon nanotubes based composites have been extensively studied which includes photoluminescence, light emission, and photonic properties etc. Single walled carbon nanotubes composites have been used in organic light emitting diode

(OLED) which have been utilized in the manufacture of thinner, brighter and power efficient displays. Recently, Nylon-6,6 based organic composites have been reported which can be used in solar cells and flexible displays. The optical properties of composites are important in dentistry as well due to the need of a material having properties (fluorescence, luminescence, opacity etc.) similar to that of a natural tooth. PMCs and composites of rare earth oxides have been found useful for dental applications. Another important aspect of optical properties is the band gap of the composites which can be engineered using different fillers and reinforcements depending upon the application [23]–[25].

1.3.5. Miscellaneous Properties

Fire retardants are self-extinguishing materials usually composed of chlorinated resins and additives like Antimony trioxide. Such materials, upon burning, release CO_2 and exhibit self-extinguishing property when the flame source is eliminated. Phenolic resins are used to make fire resistant composites but complicated post curing step and difficult handling of the material is still a problem. There are other materials which can expand and blanket the flame surface, hence preventing its spreading. Composite doors of phenolic resins have been tested, hence are possible to use in buildings as fire resistant doors [26].

A good chemical and weathering resistance makes composites a potential applicant in manufacturing chemical storage tanks, pipes, chimneys and ducts, etc. Composites like polyester resins can be used to synthesize translucent sheets and moldings with up to 85% light transmission. The non-conductive nature of these materials makes them useful for utility poles however conductivity can be induced by adding conductive additives whenever required. Composites membranes have been used as barrier films in packaging industry and also as a separator for gas mixtures [17].

1.4.   Applications of Composites

The unique properties of composites make them useful in various applications e.g. electronics, transportation, biomedical and sports etc. [27], [28].

1.4.1. Transportation

High strength and stiffness help the composites to make light weight vehicles with lower fuel consumption and payload. Composites reduce the tooling costs and can provide resistance against corrosion. The manufacturers of Mercedes and Daimler-Benz replaced glass fibers with plant fibers and jute based door panels to enhance mechanical strength, acoustic performance and energy consumption. Composites are therefore a potential candidate in automobiles industry too [18].

Primarily, composites have been used in naval application like small patrol boats' manufacture. Advanced composite materials have the potential to minimize maintenance and fabrication costs, outfit weight, enhance styling and reliability making them applicable for construction of large commercial ships [18].

Polymer composites like graphite and epoxy materials have vital role in space because of their high strength, dimension stability and specific modulus during huge temperature changes in space. Graphite and epoxy composite materials were used in the construction of SpaceshipOne which was the first privately operated vehicle launched outside Earth's atmosphere in 2004. In 2013, Airbus 350 XWB was launched having 50% composites in its structural weight. Developments in satellites, helicopters, military aircrafts, and turbine engine fan blades etc. are now being carried out by using composites of required properties [18], [23].

1.4.2. Medical

With advancement in synthetic materials, sterilization methods and surgical techniques lead to the use of composites in many ways. PMCs have attracted attention in prosthetics, sutures, joint replacement, heart valves, artificial hearts lenses and biosensors due to good biocompatibility. Rubber used in gloves and catheters is reinforced with SiO_2 particles to make it tougher and stronger. Materials such as barium glass, borosilicate glass, pre-polymerized resin and ceramic can be used as dental composites for tooth color matching and translucency [18].

1.4.3. Electronics

Currently, conducting polymer composites (CPC) have been used in electrical applications e.g. self-control heating, vapor sensing, deformation-conductivity transducers, electrostatic discharge protection and electromagnetic-radiofrequency interference shielding (EMI/RFI). Nickel coated carbon fibers are also used against EMI/RFI. CPCs consist of insulating polymer and conducting fillers; metal particles and carbon black, to attain different electrical properties. Composites can be incorporated with expensive fillers, e.g. silver or gold particles, which increase the electrical conductivity making them useful for printed circuit boards, interconnections, interlayer dielectrics, thermal interface materials, heat sinks etc.

The advancement in telecommunication industry has high demand for dielectric materials. Marett *et. al*. developed electromagnetic crystals from polymer/$BaTiO_2$ composite for microwave applications. Mica has high dielectric strength (70 MV/m), making it a useful material for insulating applications. Polymers such as polyethylene or polystyrene have dielectric strength around 20 MV/m, hence mica can be added to the polymers to increase their dielectric strength and insulating ability which is useful in capacitors, equipment for generating radio signals and in power supplies etc. [4], [18].

Apart from above mentioned applications, composites are used in construction from heavy bridges to light weight applications. Carbon fiber-reinforced cement has shown good flexural and tensile strength, resistance to wear and dimensional stability, making it useful in civil infrastructures. Earthquake-resistant buildings have been constructed using composite materials as a practical alternative for reinforced concrete frame in regions prone to earthquake. Coated and layered ballistic composites can be used in protective helmets or with ceramics for protective body armor. Sporting and leisure goods have been a huge market for PMCs. Tennis rackets, cricket bats, skis, golf clubs, and archery bows are ordinary items for carbon fiber PMCs. Wood items were replaced by steel and aluminum which are now being replaced by graphite composites. The better-quality and improved stiffness of the frame increased head size, gave additional power and reduced the weight up to 30% than their wooden version [4]. Hybrid composites are also being synthesized to further magnify the properties and applications of composites [4], [18].

1.5.   Aims and Motivation

CO_2 capture is attaining wide spread importance as a potential method for controlling greenhouse gas emissions. CO_2 increasing concentration is an important issue which has to be taken care of. A lot of research has been carried out for CO_2 capture and storage. Heavy alkaline earth metal oxides; barium and strontium have been reported to absorb CO_2 directly from the atmosphere during synthesis without the need of any complicated process. Barium carbonate is an important inorganic mineral with numerous applications in water treatment, humidity sensors, CO_2 storage etc. and requires expensive additives and precursors for the synthesis. There is a need to develop a cost effective method for the synthesis of $BaCO_3$ and to study its properties for various applications in energy storing devices.

The aim of this research is to synthesize $BaCO_3$ using simple and cost effective method. The important step is the capture CO_2 from the atmosphere for carbonate formation. Next the band gap of $BaCO_3$ will be tuned by adding CuO in different concentrations and the effect on dielectric properties of the composites will be observed. Cyclic CO_2 sorption-desorption of $BaCO_3$ needs to be studied. The effect of CuO content on carbonation and decarbonation of $BaCO_3$ is also examined in this work.

Chapter 2

Literature Review

Synthesis of inorganic materials especially oxides, carbonates and their composites have gained importance due to their electrical, mechanical, optical and industrial applications. Among the various materials, Barium Carbonate ($BaCO_3$) is an important mineral having thermodynamically stable crystal modification as compared to other heavy carbonates [29] and has close structural relationship with Calcium Carbonate (aragonite). It is odorless and white crystalline solid with little solubility in water (25mg/L at 25 °C) [30]. It has many applications in ferroelectricity, electro-catalysis, bio-mineralization etc.

2.1.   Structure and Synthesis of $BaCO_3$

$BaCO_3$ has three polymorphic forms namely orthorhombic, hexagonal and cubic. The orthorhombic phase, also known as Witherite, is the only stable form at ambient conditions. The name Witherite was given in honor of William Withering who was the first to recognize it in 1784 as a chemically distinct mineral from barites ($BaSO_4$) [31]. It undergoes transformation to hexagonal phase first (~1079 K) and then to cubic phase (~1237 K) upon thermal analysis [32]. In 2006, metastable monoclinic $BaCO_3$ was synthesized by rapid quenching during the flame spray pyrolysis method, it was reported that the monoclinic phase gets transformed to stable orthorhombic phase after few days at room temperature [33]. Figure 2.1 and 2.2 shows the 2D and 3D structure of $BaCO_3$ respectively.

Figure 2.1: 2D structure of $BaCO_3$.
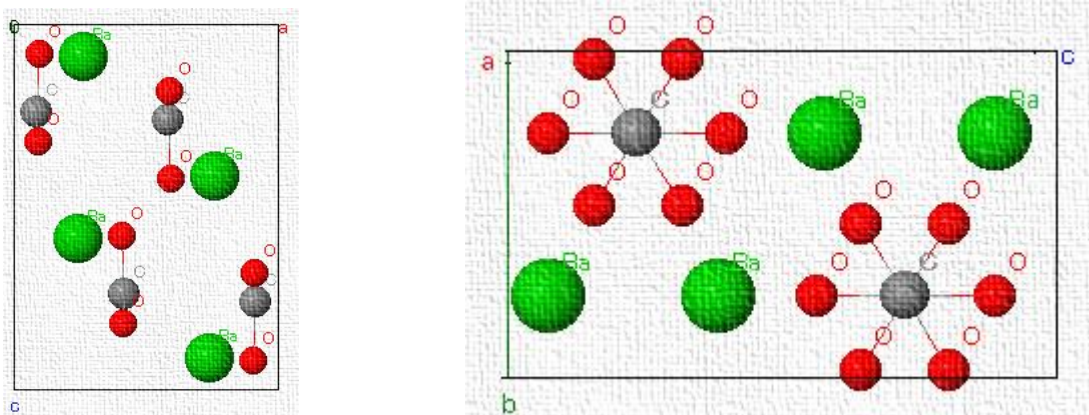
Figure 2.2: Different views of orthorhombic BaCO₃ unit cell.

To date, various methods have been reported for the synthesis of $BaCO_3$. Commercially, soda ash method is used in which barium sulfide is treated with Na_2CO_3 at 60 to 70 °C or by passing CO_2 at 40 to 90 °C; obtained precipitates are washed and dried. Reaction mechanism is given by [30].

$$BaS + Na_2CO_3 \rightarrow BaCO_3 + Na_2S$$

$$BaS + CO_2 + H_2O \rightarrow BaCO_3 + H_2S$$
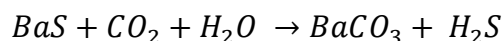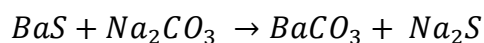
Other methods include precipitation, hydrothermal, sol-gel, microemulsion, sonochemical and polymer assisted methods [34]–[39] etc. In polymer assisted method, the effect on morphology is prominent e.g. Polyacrylamide assisted method was responsible for the shape evolution process starting from nanocuboid-spheres to dumbbell while Polyethylene glycol assisted method was reported to form dendritic structures [40], [41]. Apart from polymers, pH, certain surfactants and additives also affect the morphology of $BaCO_3$ particles [37], [42]. All these mentioned methods are useful for diversity in the morphologies and particle sizes which play important role in defining the properties and applications of $BaCO_3$.

2.2. Properties and Application of $BaCO_3$

$BaCO_3$ has wide range of uses and applications discussed in this section. It is mixed with wet clay to make uniform red bricks by immobilizing water-soluble salts. It improves the refractive index of optical glass and also makes glass bead formation easier by promoting sintering and lowering viscosity of molten glass. It acts as a flux in ceramic industry for glazes and enamel. $BaCO_3$ inhibits coagulation in ferrous metallurgy, removes sulfates in Chlor-Alkali cells for purifying brine. The most important use is the synthesis of other inorganic barium salts in which it acts as Ba-precursor [30]. In 2006, hexagonal whiskers of $BaCO_3$ were synthesized which showed good tensile strength and can be used in fiber reinforcement for high stress applications [38].

- *Coating Applications*

Now-a-days epoxy powder coatings are extensively used due to having unique dielectric, corrosion and mechanical properties but these materials lag behind in toughness for which ceramic-based fillers are used to fill up the weak point. $BaCO_3$ is used as inert filler to improve thermal curing of epoxy/1,8-naphthalene diamine system. A substantial increase in the glass transition temperature from 85 to 100 ^{o}C was observed for optimum composition [43].

- *Solid Oxide Fuel Cells (SOFCs)*

Oxygen reduction reaction (ORR) in the cathodes governs the performance of SOFCs. The performance can be improved by increasing the surface area of the electrode where ORR takes place. $BaCO_3$, being thermally stable and chemically compatible, has demonstrated excellent catalytic activity by increasing surface area for high temperature ORR on $La_{0.8}Sr_{0.2}FeO_{3-d}$ (LSF) cathode for SOFCs due to which these cathode showed enhanced and stable electrochemical performance with minor perturbations [44].

- *Anticancer Activity*

Recently, $BaCO_3$ have been synthesized via green route using aqueous extract of *Mangifera indica* seed as reducing agent. It was reported that $BaCO_3$ particles increased the activity of caspase-3 (enzyme) which promotes apoptosis (cell death) thus the particles were found as a promising agent against cervical carcinoma (cervix cancer). The concentration of $BaCO_3$ had to be monitored because high concentration was found to be harmful for normal cells. This synthetic route was rapid, in-expensive, and eco-friendly for development of multifunctional particles for cancer treatment [45].

- *Water Treatment*

$BaCO_3$ is useful for sulfate removal from pre-treated mine water. The rate of sulfate removal showed an increase with increasing $BaCO_3$ concentration but the sulfate must be associated with calcium as it removes the carbonate linked with the barium cation. Barium Sulfate and Calcium Carbonate are co-precipitated and removed via filtration [46].

$$BaCO_3 + Ca^{2+} + SO_4^{2-} \rightarrow BaSO_4 + CaCO_3$$
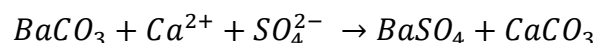
- *Sensors*

For the first time in 2015, Composite Hydroxide Mediated (CHM) method was used to synthesize $BaCO_3$ nanowires which were found to be good for humidity sensors. The change in humidity was measured in terms of change in resistance i.e. increase in humidity resulted in decreased resistance of $BaCO_3$ nanowires. It was found that the shape of the nanowires aids the adsorption and desorption of water molecules as well as gives them edge in their quick recovery and response to humidity. Thus, $BaCO_3$ nanowires can be used in humidity control electronic devices and in monitoring highly sensitive environments [47].

2.3.   Composites of BaCO$_3$ with Transition Metal Oxides (TMO)

Several reports have been found on the composites of BaCO$_3$ with TMO. The most commonly studied is the Barium Titanate (BaTiO$_3$) which is an important ferroelectric material with wide applications in resistors, transducers, piezoelectric devices and semiconductors. It exists in five different crystallographic forms such as cubic, hexagonal, orthorhombic, tetragonal and rhombohedral. The first two forms i.e. hexagonal and cubic are paraelectric (temporary polarization) while orthorhombic, tetragonal and rhombohedral are ferroelectric in nature. The strongly basic nature of BaCO$_3$ modifies TiO$_2$ and improves its performance in dye sensitized solar cells. It basically shifts the conduction band of TiO$_2$ in negative direction ultimately increasing its conversion efficiency. Doping is important for attaining required characteristics for certain application and the perovskite structure of BaTiO$_3$ makes it easier to incorporate ions of different sizes thereby allowing variety of dopants to be easily accommodated e.g. ZrO$_2$ doping improved the dielectric properties of BaTiO$_3$ [48]–[54]. BaCO$_3$/Fe$_2$O$_3$ is another important composite synthesized via mechanical alloying in which grain size is important in determining the magnetic properties. BaCO$_3$ enhances the magnetization of nano-ferrites which makes them useful for hard magnetic applications. It induces phase transformation which modifies the structure and also transforms the magnetic response (ferromagnetism). This method is useful for synthesizing permanent barium hexaferrite materials which are suitable for magneto-electric devices. By carefully controlling the dielectric properties Barium Ferrites can be used as supercapacitors and in microwave applications apart from these, they are also used in barcode and recording devices [55]–[58]. Recently, Cobalt (Co) modified NiO/BaCO$_3$ catalyst for N$_2$O decomposition has been reported. It was found that on introducing BaCO$_3$, the surface area and the actives sites were increased which improved the conversion efficiency of Co-incorporated NiO while in its absence, the surface area was decreased along with the catalytic efficiency [59]. In 2014, ZnO/BaCO$_3$ composite was synthesized via sol-gel

method and optical properties were studied. Addition of $BaCO_3$ increased the crystallite size of composite which showed red shift and the band gap was decreased from 3.30 to 3.26 eV on increasing $BaCO_3$ concentration in the sample [60].

Barium Niobate ($BaNbO_3$), synthesized via composite hydroxide mediated method using $BaCO_3$ and Nb_2O_5, has been found to be an excellent candidate for humidity sensing electronic devices. It acts as a superconductor at 18.6 K and has been used as a precursor for the synthesis of $Sr_xBa_{1-x}Nb_2O_6$ (0.25 $<x<$ 0.75) which is a ferroelectric ceramic material. $BaNbO_3$ has higher stability and anticorrosion ability and is also used in chemical sensors, multilayer ceramic capacitors, chemical and nonvolatile memories [61]–[66]. Barium Zirconate ($BaZrO_3$), like other Barium composites, exhibits perovskite structure and is of great importance in high temperature applications. It is thermally stable and does not undergo phase transition from 1327 °C down to -269 °C which makes its suitable for thermal barrier coating applications. It is also used as a container for growing crystals of high Tc superconductors like Yttrium Barium Copper Oxide (YBCO) because of its chemical inertness with them [67], [68]. Along with $BaZrO_3$, Barium Cerate ($BaCeO_3$) is used for better protonic conduction. $BaCeO_3$ is unstable in CO_2 atmosphere so $BaZrO_3$ is added to improve its stability. Due to high temperature ionic conduction, it is used in hydrogen gas sensors, hydrogen production and in intermediate temperature (500-750 °C) solid oxide fuel cells (IT-SOFCs) [69], [70].

2.3.1. $BaCO_3$/CuO Composites

$BaCO_3$ and CuO have been used for the synthesis of $BaCuO_x$ based high Tc superconductors namely Yttrium Barium Copper Oxide commonly known as YBCO. It was found that in synthesizing YBCO, CuO acts as a catalytic agent for the decarbonation of $BaCO_3$ and results in the formation of $BaCuO_2$. The effect of carbon on YBCO was demonstrated and it was reported that increasing amount of carbon in the

samples resulted in highly microporous structures. Shogo *et. al.* fabricated CO_2 sensors using $CeO/BaCO_3/CuO$ ceramics which have high resistance to humidity and can be used in indoor quality monitoring systems [71]–[73].

To the best of our knowledge, simple $BaCO_3/CuO$ composites, their physical properties and cyclic heat treatment of $BaCO_3$ have not been reported till yet. The combination of an insulator ($BaCO_3$) and a semiconductor (CuO) will amalgamate their properties leading to a material with new applications in optical and electronic devices.

Chapter 3

Experimentation and Characterization

3.1.   Synthesis

In this section, the synthesis of $BaCO_3$, CuO and their composites via simple co-precipitation method [74] with modified thermal conditions has been discussed.

The synthesis of $BaCO_3$ was carried out at room temperature. The following reagents were used without further purification:

- Barium Nitrate ($Ba(NO_3)_2$) (RDH grade with purity $\geq$99%)

- Sodium Hydroxide (NaOH) (99.9%)

- Distilled Water

0.1 M aqueous solution of $Ba(NO_3)_2$ was prepared and 0.8 M $NaOH_{(aq)}$ was added dropwise to get white precipitates. The solution was stirred at 60 °C for 4 h and then for 24 h at room temperature to prevent agglomeration of particles and to ensure the maximum absorption of CO_2 from the atmosphere. The obtained precipitates were centrifuged at 10,000 rpm for 10 mins followed by washing with water. Later they were vacuum dried at 150 °C for 2 h. The dried precipitates were then annealed at 500 °C for 4 h to completely remove the impurities and increase the basic site.
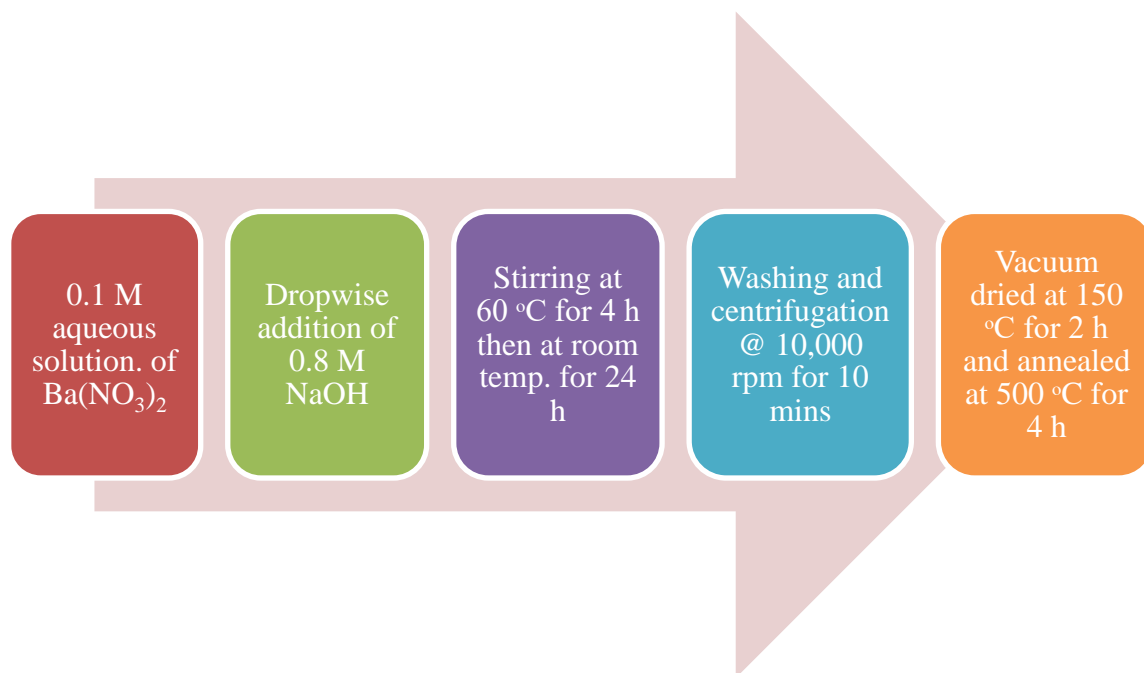
Figure 3.1: Flowsheet for the synthesis of BaCO$_3$ particles.

Similar method was used for the synthesis of CuO particles. The reagents used are:

- Copper Nitrate Trihydrate (Cu(NO$_3$)$_2$.3H$_2$O) (RDH grade with purity $\geq$99%)
- Sodium Hydroxide (NaOH) (99.9%)
- Distilled Water

0.1 M aqueous solution of Cu(NO$_3$)$_2$.3H$_2$O was prepared to which 0.8M NaOH was added dropwise resulting into black precipitates indicating the formation of CuO particles. The mixture was stirred followed by washing and centrifugation at 10,000 rpm for 10 mins twice with water and then with ethanol for complete removal of impurities. The precipitates were dried in vacuum oven at 150 °C for 2 h and annealed at 600 °C for 4 h.

0.8 M NaOH dropwise addition forming black ppt.

0.1 M $(Cu(NO_3)_2.3 H_2O)$ (aq)

Washed, centrifuged, @ 10,000 for 10 mins

Dried at 150 °C for 2 h and annealed at 600 °C for 4 h.
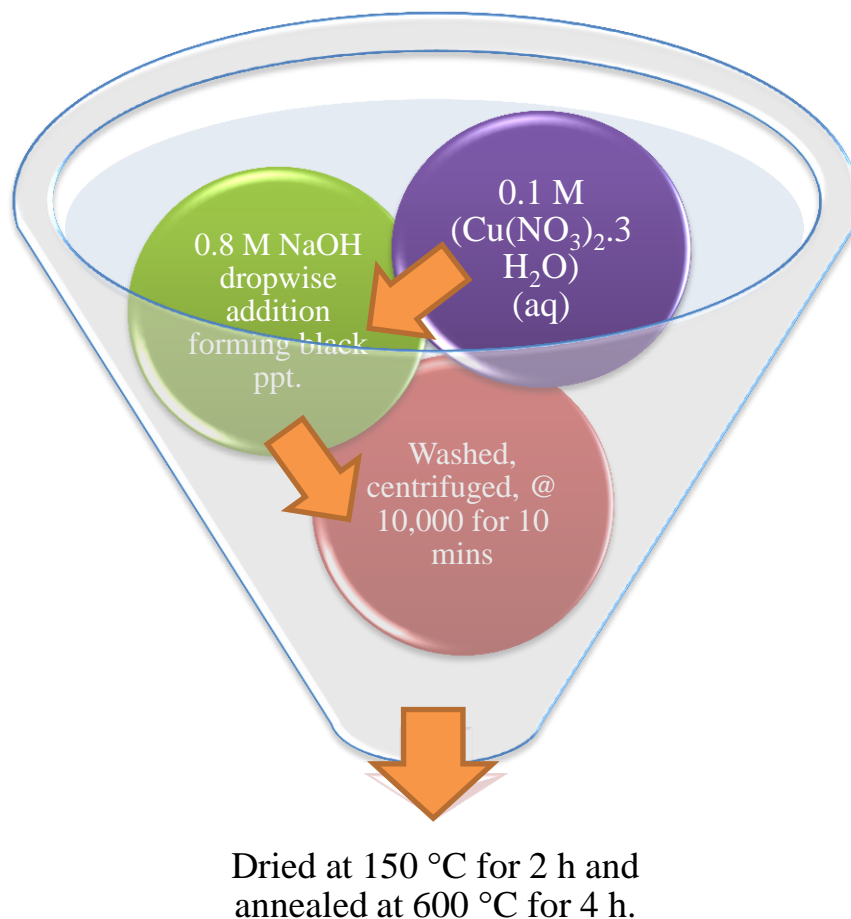
Figure 3.2: Schematic synthesis of CuO particles.

As synthesized $BaCO_3$ and CuO dry powders were used for the preparation of composites. The two powders were ground together in different concentrations as shown in table 3.1. The ground mixture was then pelletized via hydraulic press using a 10 mm (internal) diameter stainless steel die under a pressure of 5 tons. The pellets were then analyzed for further characterization.

Table 3.1: (BaCO₃/CuO) composites w/w % compositions.

Composites	Composition (w/w %)	
	BaCO$_3$	**CuO**
A	80	20
B	60	40
C	40	60
D	20	80

3.1.1. Synthesis Chemistry

The metal salts of barium and copper are completely soluble in water forming clear solutions. On the addition of NaOH (pH = 12), precipitation occurs and the hydroxide of copper is formed while in case of barium the atmospheric CO_2 is absorbed by the sample and carbonate is produced.

$$Ba(NO_3)_{2\,(aq)} + 2NaOH + CO_{2\,(atmosphere)} \rightarrow BaCO_{3\,(ppt)} + 2NaNO_3 + H_2O$$

$$Cu(NO_3)_2 \cdot 3H_2O_{(aq)} + 2NaOH \rightarrow Cu(OH)_{2\,(ppt)} + 2NaNO_3 + 3H_2O$$
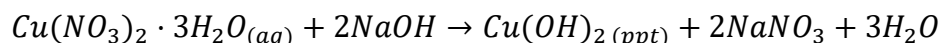
The nitrates ($NaNO_3$) got removed by washing and centrifugation whereas thermal treatment led to the removal of excess water. Copper hydroxide was converted to copper oxide by annealing to remove OH⁻ ions.

$$Cu(OH)_2 \xrightarrow{\Delta} CuO + H_2O$$
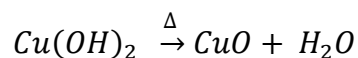
3.2.   Characterization

The crystal structures of the prepared samples were examined by X-Ray powder diffraction, XRD (STOE Germany) with Cu-Kα (λ = 1.5418 Å) as radiation source operating at 40 kV and 40 mA current, the 2θ range is 20° to 80°. The powder pattern was identified using the database incorporated in the software.

The Morphological analysis was done by using field emission scanning electron microscopy (FESEM model MIRA3 TESCAN Zeiss Supra 55 VP) equipped with an EDX system operating at 10 kV and magnification is 25 kx. As the samples were non-conducting so they were sputtered on a carbon tape, and coated with graphite. The stubs were then placed in the vacuum chamber for imaging. Fourier transform infrared (FTIR) spectroscopy was employed to measure the vibration frequencies for all the samples. FTIR analysis was carried out using BRUKER-Germany model ALPHA with spectral range 4000 to 550 cm^{-1}. The machine was equipped with platinum ATR so no sample preparation was required. A small amount of powder sample was placed on the diamond sensor and pressed into a small pellet and spectrum was recorded. Thermogravimetric analysis (TGA) was done using Mettler Toledo STAR System having 0.005% temperature accuracy. The sample was placed in alumina holder. It was thermally treated from 25 °C to 1500 °C at the rate of 10 °C/min under air.

Optical properties were measured using Perkin Elmer UV/VIS/NIR spectrometer Lambda 950 with the spectral range of 190-3300 cm^{-1}. The powder sample was placed in holder to scan the reflectance spectra. For measuring the dielectric properties LCR meter (Wayne Kerr model 6500B) having frequency range 100 Hz to 5 MHz was used. The sample pellets were fixed between the electrodes one by one for data recording. All the measurements were carried out at room temperature.

Chapter 4

Results and Discussion

4.1.   X-ray Powder Diffraction (XRPD)

X-ray powder diffraction has been done to analyze the crystal data and the phase of the prepared samples. The XRPD (figure 4.1) of prepared $BaCO_3$ sample shows that it is a single phase material and its peaks matched with witherite (ICSD card no. 00-045-1471) [75] indicating that Ba sample successfully absorbed CO_2 at ambient conditions. The diffraction peaks are indexed to orthorhombic witherite i.e. $BaCO_3$ having space group *Pnma* (no. 62) with lattice constants, a = 6.4300, b =5.3140, c = 8.9040 Å. The most prominent peak at 23.9° correlates with hkl indices (111) of orthorhombic $BaCO_3$ structure (witherite) signifying that its crystals primarily grow along the (111) face. The XRPD of CuO shows that it is also single phase and has monoclinic symmetry and space group $C2/c$ (no. 15) with lattice constants; a = 4.6853, b = 3.4257, c = 5.1303 Å, β = 99.54°. All the diffraction peaks are perfectly indexed to tenorite (ICSD card no. 00-045-0937) [76].

The powder patterns of the composites show diffraction peaks of both CuO and $BaCO_3$ confirming the presence of both phases. The intensity of the diffraction peaks at 23.9°, 34.1° and 34.5° decrease with decreasing $BaCO_3$ concentration while the intensity of CuO diffraction peaks at 35.5° and 38.7° increases on increasing the CuO concentration. There was no extra peak found in the patterns indicating the purity of phases.
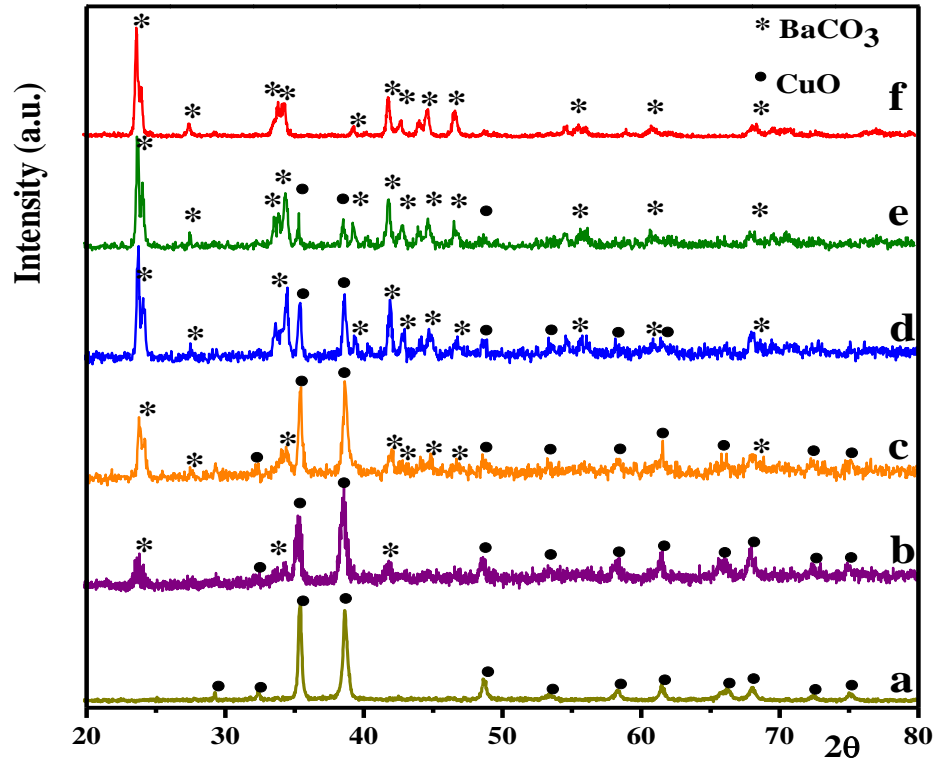
Figure 4.1: XRPD patterns of; (a) BaCO₃, (b-e) Composites (BaCO₃ 80%, 60%, 40%, 20%), and (f) CuO.

The crystallite size and lattice strain can be obtained from peak width analysis of the samples. The crystallite size can be determined by using Debye-Scherrer's equation [77]

$$D = \frac{k\lambda}{\beta_D cos\theta}$$

Where D is the crystallite size, k is the shape factor (0.94), λ is the wavelength of the Cu-Kα, β represents the full width at half maxima and θ is the Bragg diffraction angle. However this formula does not consider the peak broadening (β_D) due to lattice strain and instrumental error; for which Cullity devised a formula which considers the contribution of instrumental error to the broadening of diffraction peak [78].

$$\beta = \sqrt{\beta_{exp}^2 - \beta_{standard}^2}$$

The stress induced broadening (β_ε) is linked to residual stress (ε) that is given by Wilson formula [79].

$$\beta_\varepsilon = 4\varepsilon \tan\theta$$

So, the observed broadening is simply the contribution of both; sample crystallite size and micro strain [79].

$$\beta = \beta_D + \beta_\varepsilon$$

$$\beta \cos\theta = \frac{k\lambda}{D} + 4\varepsilon \sin\theta$$

Williamson and Hall formulated the effect of micro strain on peak broadening by plotting $(\beta\cos\theta/\lambda)$ *vs* $(\sin\theta)$ [78]. The slope of the WH-plot gives the value of micro strain. The positive slope corresponds to lattice expansion, while negative slope specifies lattice compression and if the sample consists of a perfect crystal, a horizontal slope is obtained indicating the absence of micro strain [80]. Table 4.1 gives the comparison of crystallite size calculated using the Debye-Scherrer formula and WH-plot.

Table 4.1: Crystallite size calculated from Debye-Scherrer formula and WH plot.

Sample	Average Crystallite Size (nm)*	Crystallite Size (nm)[#]	Lattice Strain (%)
$BaCO_3$	52.4	46	0.6(1)
CuO	86.5	82.5	0.3(1)

*calculated from Debye–Scherrer formula.
calculated from WH-Plot.

The WH-plot of $BaCO_3$ and CuO shows a positive slope indicating lattice expansion which may be due to the point defects, surface stress or formation of oxygen vacancies that reduces the electrostatic bonding force [81].
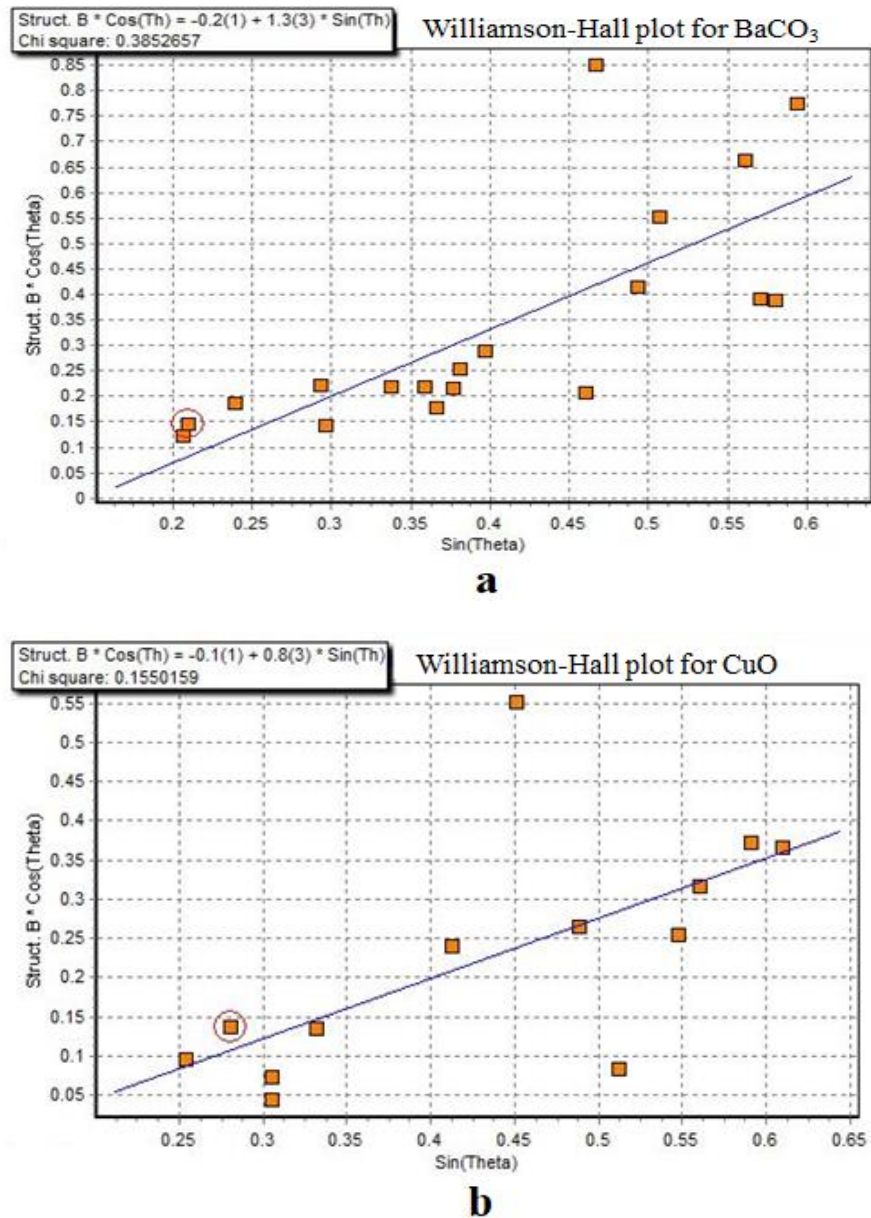
Figure 4.2: Williamson-Hall plot for (a) BaCO₃ and (b) CuO.

4.2.   Field Emission Scanning Electron Microscopy (FESEM)

For morphological analysis, the prepared samples were subjected to FESEM analysis. Figure 4.3a shows FESEM image of $BaCO_3$ particles having spherical morphology in which the bulk particles are agglomerated due to hygroscopic behavior of the sample. The average particle size was found to be ~200 nm. CuO particles are shown in figure 4.3b they are also spherical with average particle size of ~150 nm. The difference in the particle and crystallite size is due to polycrystalline agglomeration. The crystallite size can be said to correspond to the size of a crystal inside the particle [82].
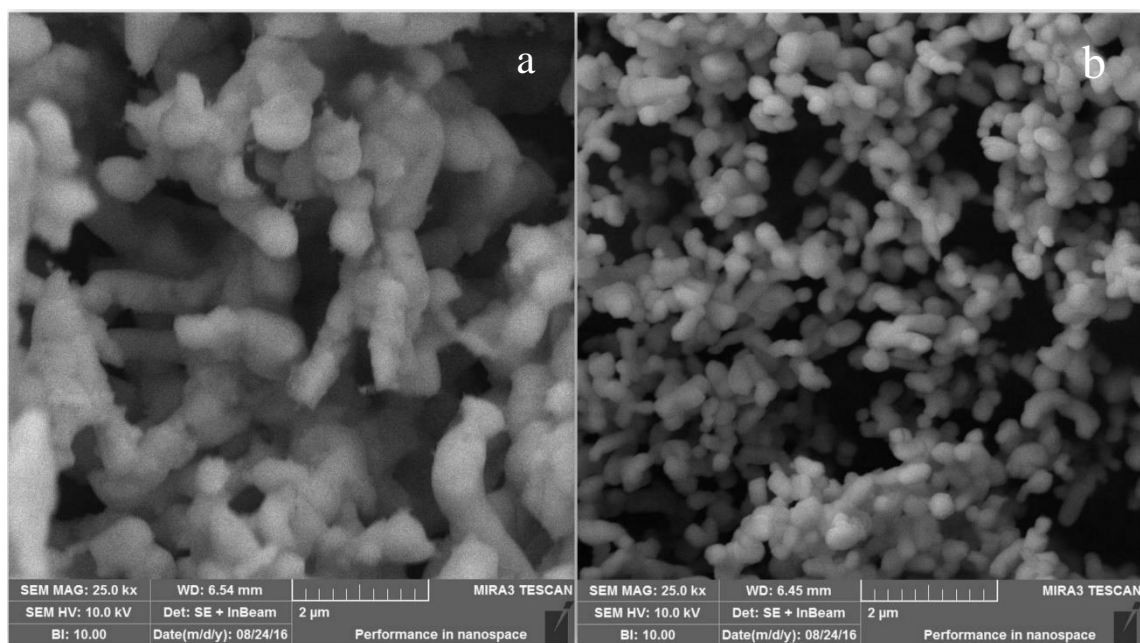
Figure 4.3: FESEM images (a) BaCO₃ particles (b) CuO particles.

The elemental analysis was carried out by EDX equipped with FESEM. Figure 4.4a shows EDX spectra of $BaCO_3$ indicating that the sample contains Ba, C and O while figure 4.4b shows EDX spectra of CuO, confirming the presence of both elements i.e. Cu and O. The obtained results further verified the purity of the samples and the extra peaks can be attributed to the coating material (gold and graphite respectively).
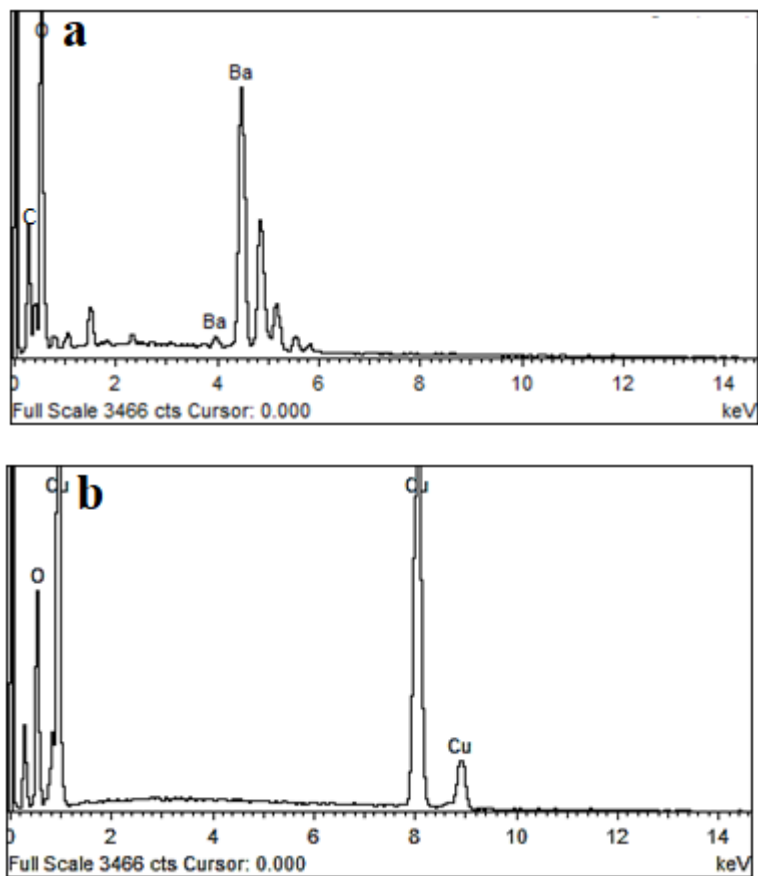
Figure 4.4: EDX Spectra; (a) BaCO₃, (b) CuO.

4.3. Fourier Transform Infrared Spectroscopy (FTIR)

FTIR analysis has been employed for the analysis of chemical bonds in a molecule to confirm the reaction of CO_2 and Ba sample. The IR band at 1411.02 cm^{-1} corresponds to the asymmetric O-C-O bond stretching i.e. unidentate carbonates that are formed due to the strong association of CO_2 with the basic sites of BaO as these associations require surface basic oxygen atoms [83] (figure 4.5). The small band at 1750.62 cm^{-1} is due to bridging carbonates stretching [84] while the band at 1059.54 cm^{-1} can be attributed to

symmetric O-C stretching. The sharp bands at 855.97 and 692.69 cm^{-1} are out plane and in plane bending vibrations of carbonates (CO_3^{2-}) respectively [85], [86].
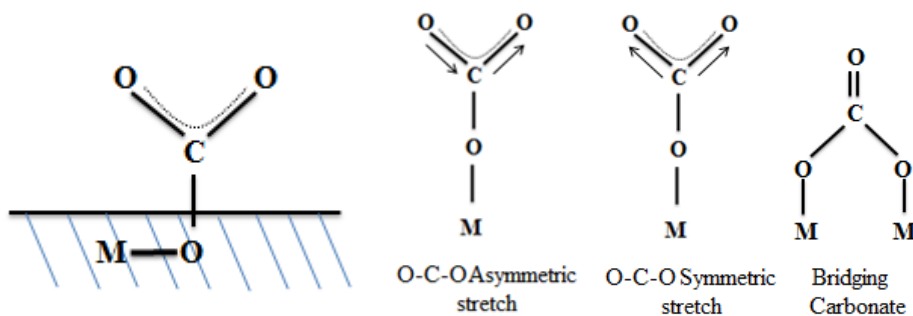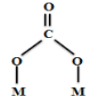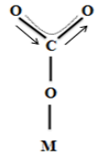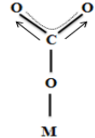
Figure 4.5: Unidentate carbonate vibrations (strong basic site due to surface oxygen atoms).

The IR bands of absorbed CO_2 at room temperature are summarized in table 4.2.

Table 4.2: Wavenumbers of absorbed CO_2 vibration bands and their assignment.

Assignment		Wavenumbers of IR bands (cm^{-1})
Bridging Carbonate and CO_2 stretching		1750 [84]
Unidentate O-C-O asymmetric stretching		1411 [85]
Unidentate symmetric O-C stretching		1059 [84]
Out of plane bending of carbonate		855 [86]
In plane bending carbonate		692 [86]

The peaks in the range 590-605 cm^{-1} and 1300-1380 cm^{-1} are attributed to Cu-O stretching and bending vibration respectively. The FTIR results of all samples are compared in figure 4.6. It can be seen from the spectra that the composites show reduced intensity of O-C-O band (asymmetric stretching) due to decreasing $BaCO_3$ concentration and the transmittance of the sample decreases due to increasing CuO concentration also indicated by the reduced intensity of the bands in 590-600 cm^{-1} region as seen in the figure below.
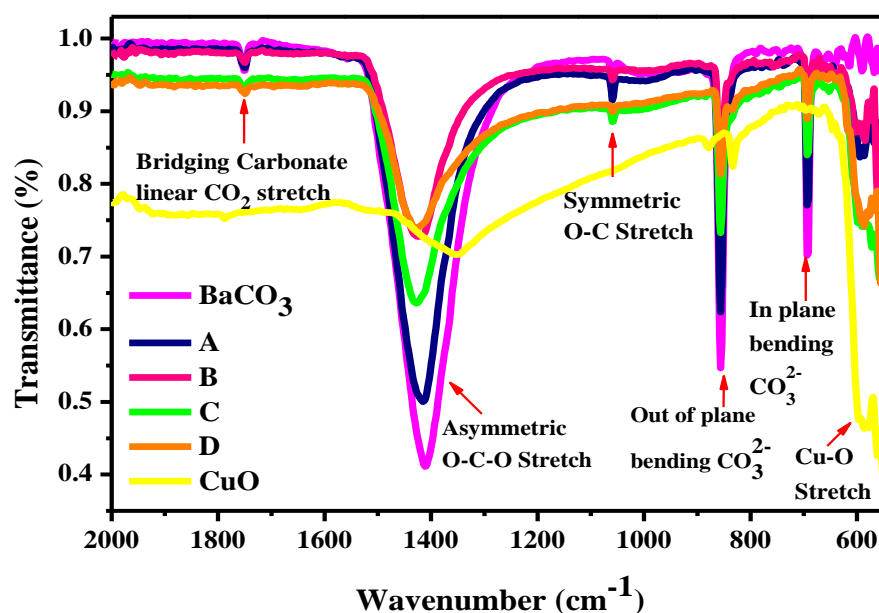
Figure 4.6: FTIR of BaCO₃, CuO and composites (BaCO₃; A: 80%, B: 60%, C: 40%, D: 20%).

4.4.   Thermogravimetric Analysis (TGA)

Thermal analysis was carried out to find the decomposition temperature of $BaCO_3$ as well as the temperature at which CO_2 is evolved from $BaCO_3$ which will confirm whether the CO_2 is absorbed or adsorbed on the sample. The TG curve (figure 4.7) shows a slanting

line initially indicating the removal of moisture from the sample also shown by the downward DTA peaks which correspond to endothermic reaction (weight loss). A prominent step is observed at 902.33 °C accounting for the loss of CO_2 from the sample. The total mass loss from the sample was 23% during 25 °C to 1150 °C temperature interval which is contributed to the moisture and CO_2 loss together. $BaCO_3$ exhibits two phase conformations; a downward DTA peak near 800-810 °C indicates orthorhombic to hexagonal phase transformation while peak in the range 1050-1100 °C specifies hexagonal to cubic phase change of $BaCO_3$ i.e. the formation of BaO [32]. On further heating till 1500 °C the sample was degraded.

$$BaCO_{3\,(s)} \xrightarrow{\Delta} BaO_{(s)} + CO_{2\,(g)}$$
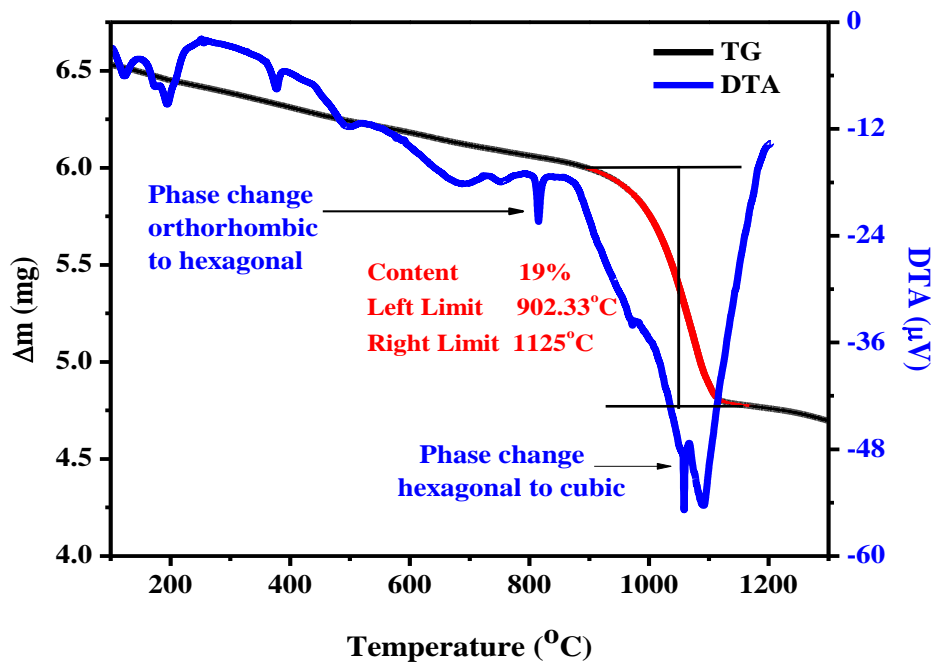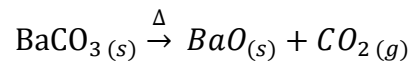
Figure 4.7: TGA/DTA curve of $BaCO_3$.

45

To further confirm the TGA results, FTIR of the sample was performed at temperatures which indicated CO_2 loss. The $BaCO_3$ sample was placed in silica crucible and heated to 900 °C for 10 min in the muffle furnace at the rate of 10 °C/min under air. After achieving the required temperature the furnace was cooled at the same rate to room temperature. Once the sample was cooled, the FTIR was taken immediately, similar procedure was followed for 1000 °C and 1100 °C and the results were compared (figure 4.8).
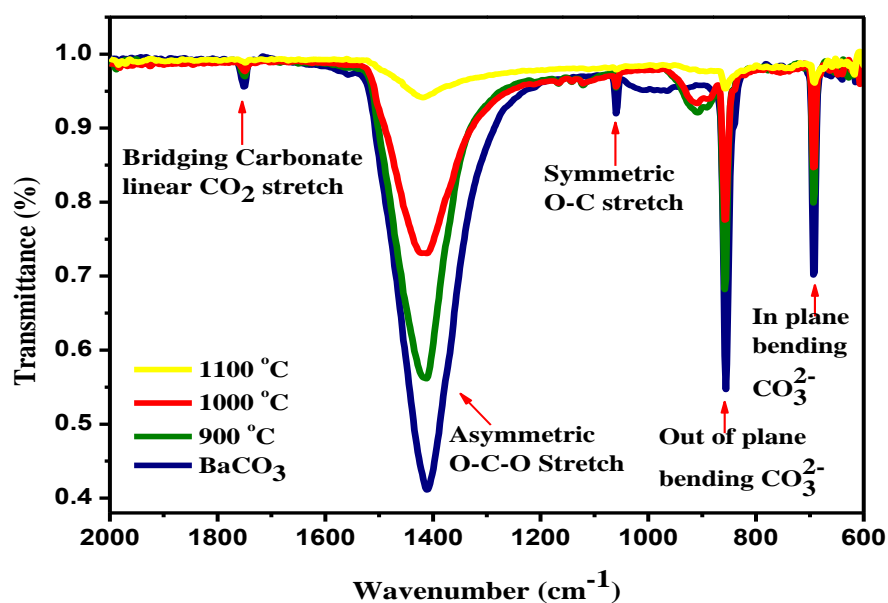
Figure 4.8: FTIR of BaCO₃ sample heated at different temperatures.

It is clear from the spectra that the samples reabsorbed CO_2 on cooling but the absorption efficiency decreased when the sample was heated at higher temperatures i.e. 1000 °C and 1100 °C as indicated by the reduced intensity of O-C-O stretching bands. It can be concluded that above 1100 °C the sample did not absorb CO_2 and the absorption property degrades with increasing temperature.

4.4.1. Cyclic CO_2 Sorption-Desorption of $BaCO_3$

Pure $BaCO_3$ was subjected to cyclic heat treatment for examining the absorption desorption behavior. FTIR of the sample was carried out prior to heating and then the sample was heated at 900 °C for 2 h followed by FTIR analysis. Similar procedure was carried out for the same sample for 3 days, FTIR was carried out before and after heating, and the spectra were recorded.
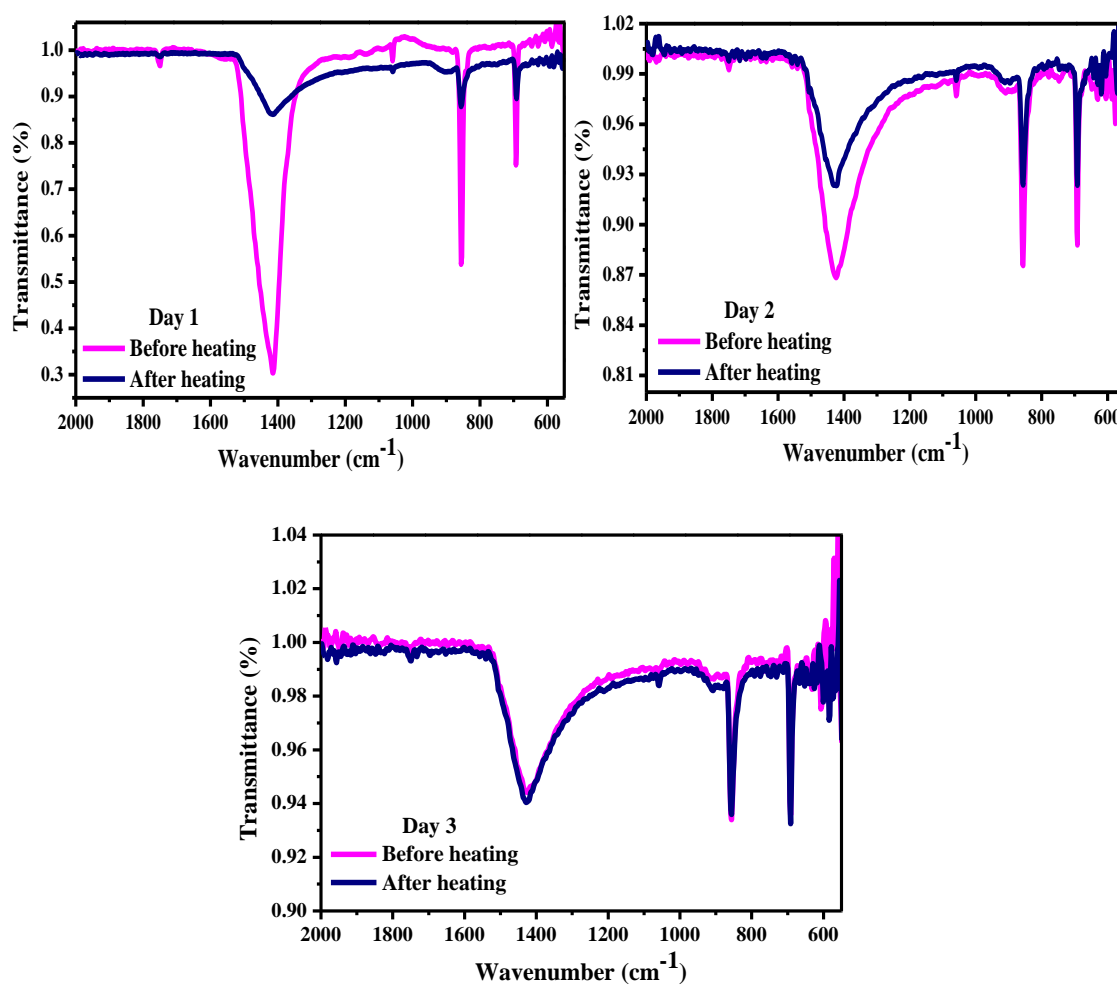
Figure 4.9: Cyclic CO_2 sorption-desorption of $BaCO_3$.

It can be seen from figure 4.9 that after annealing on day 1 the O-C-O stretching band shows a sharp decrease in intensity indicating a decreased reabsorption behavior which corresponds to the previous FTIR results. High temperature and prolong heating induces sintering agglomeration in the sample which leads to reduced absorption efficiency [87]. The intensity of the band did not decrease sharply on day 2 and on day 3 the intensity remained almost same before and after heating indicating that the sintering is complete and $BaCO_3$ retains its absorption behavior after 3 cycles. It can be concluded that the CO_2 may be trapped inside the bulk of sample and higher temperature is required for desorption.

4.4.2. CO₂ Sorption/Desorption Experiment

$BaCO_3$ and composite A (80% $BaCO_3$:20% CuO) were subjected to CO_2 sorption desorption experiment to observe the effect of CuO. Desorption was carried out by heating the sample to 950 °C at the rate of 10 °C/min for 90 min under ambient conditions. The sorption was carried out by decreasing the temperature to 700 °C at the rate of 10 °C/min under CO_2 atmosphere with holding time of 30 min. Figure 4.10 indicates that TG curve of $BaCO_3$. A fluctuation in weight loss is observed above 900 °C which shows that CO_2 is not completely evolved from the sample due to the formation of liquid phase ($BaCO_3$ + BaO) as a result of eutectic reaction. At and above the eutectic temperature, $BaCO_3$ dissolves the BaO (formed below eutectic temperature) and results in a liquid layer at the surface of unreacted $BaCO_3$, forming a three phase equilibria; BaO-liquid-$BaCO_3$ (figure 4.11). The CO_2, produced due to decomposition, is dissolved in this liquid phase forming CO_3^{2-} ions thereby, arresting the further loss of CO_2 from the sample [32]. When the sorption cycle begins, the weight loss is regained by the sample indicating the reabsorption of CO_2 from the atmosphere.
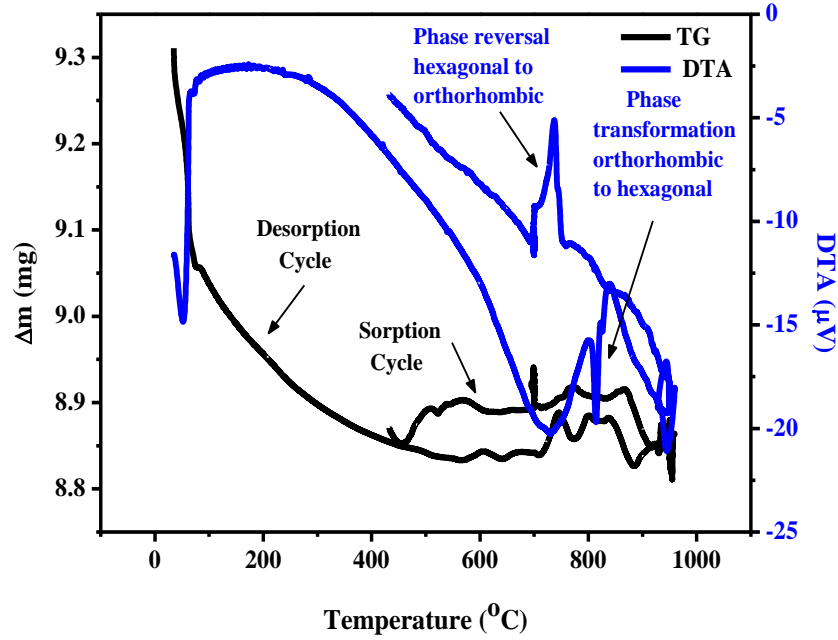
Figure 4.10: Carbonation/Decarbonation cycle of BaCO₃.
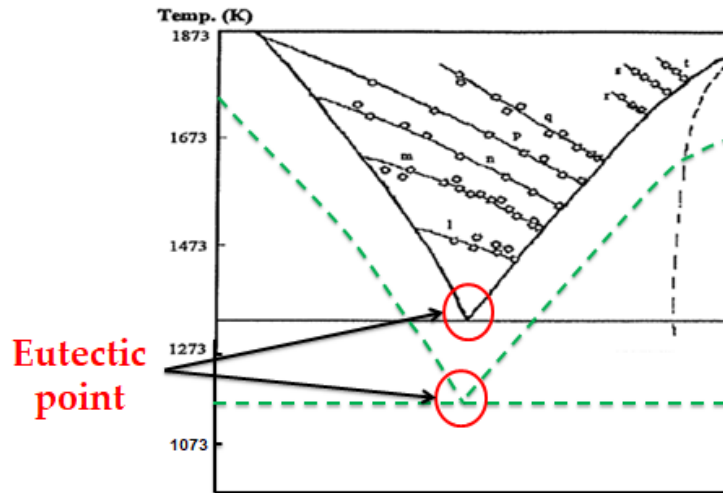
Figure 4.11: Binary phase diagram for BaO-Liquid-BaCO₃ equilibria. Black lines represent reported data [32] while green dotted line represents data for this work.

Similar procedure was repeated for composite A (figure 4.12). It was observed that during the sorption cycle the composite did not regain the weight lost during desorption which depicts the formation of an intermediate compound. It is reported that CuO aids in the removal of CO_2 and reacts with the BaO produced due to decomposition of $BaCO_3$ and results into the formation of $BaCuO_2$ which does not reabsorb CO_2 [72]. Hence the TG curve does not meet at the initial point of weight loss.
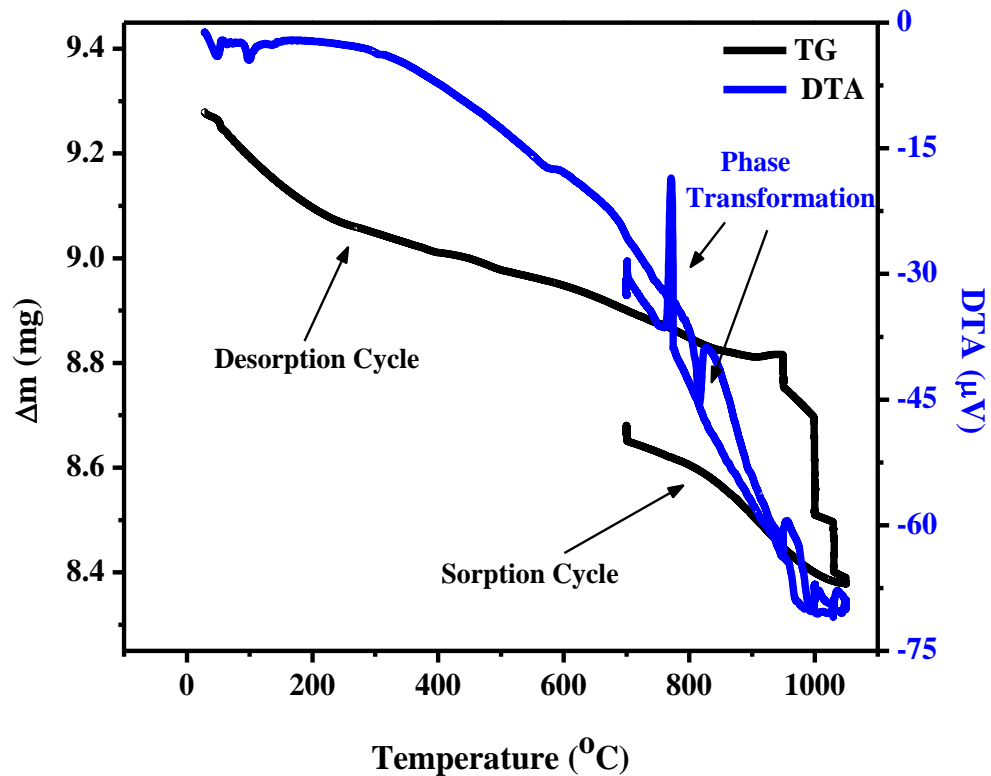
Figure 4.12: Carbonation/Decarbonation of Composite A (80% BaCO₃:20% CuO).

The formation of $BaCuO_2$ was confirmed by XRPD of CA after heating at 900 °C for 2 h. It can be seen in figure 4.13 that the sample consists of multi-phases; $BaCuO_2$ (ICSD card no. 00-038-1402), $BaCO_3$ and CuO. The reduced intensity of $BaCO_3$ and CuO

peaks confirms the reaction leading to the formation of $BaCuO_2$ which arrests the CO_2 reabsorption as explained by the TGA curve so further sorption desorption experiments were not performed.
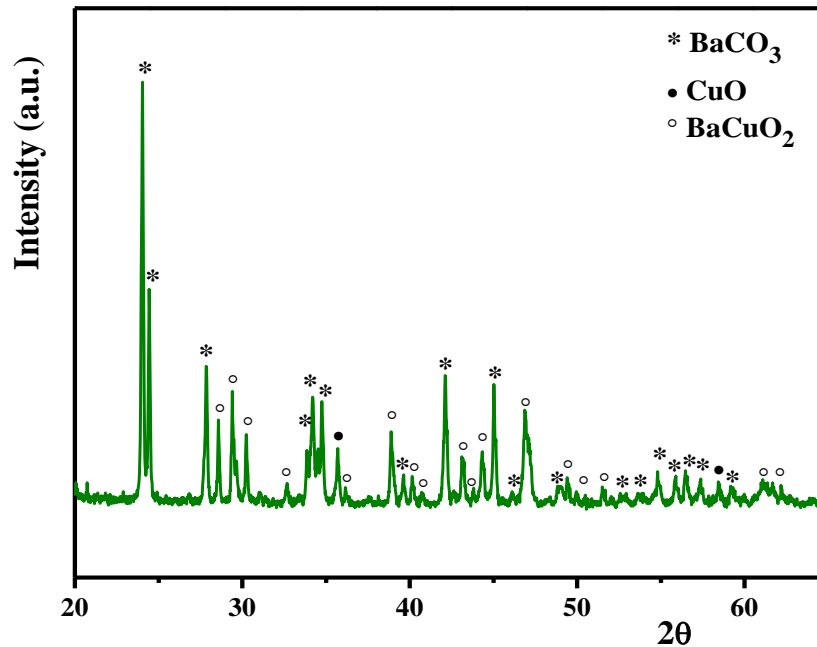
Figure 4.13: XRPD of CA (80% $BaCO_3$:20% CuO) after heating.

4.5.   Properties

The composites of $BaCO_3$/CuO were prepared to study the effect of concentrations of CuO on the optical and dielectric properties of $BaCO_3$. The properties are discussed below.

4.5.1. Optical Band gap

The optical band gap of the samples was calculated via UV-Vis analysis in diffuse reflectance mode in the range 200-1000 nm. Figure 4.14 shows the % reflectance vs

wavelength plot. $BaCO_3$ showed reflectance in the ultraviolet and infrared region while CuO showed reflectance in the ultraviolet region around 300 nm.
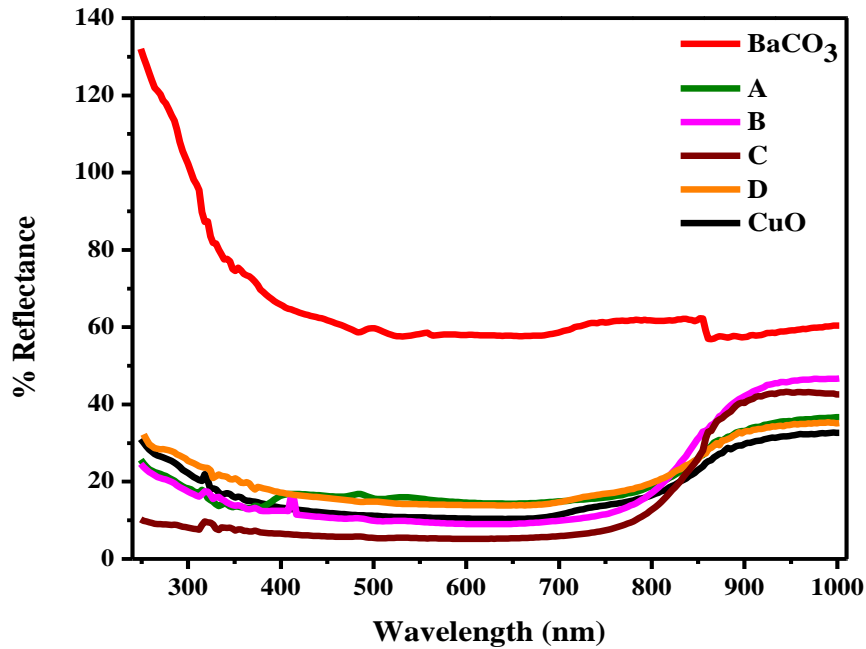
Figure 4.14: Reflectance spectra of BaCO$_3$, CuO and Composites ((BaCO$_3$; A: 80%, B: 60%, C: 40%, D: 20%).

The Band gap energy (E_g) values are calculated from Kubelka-Munk equation [77]

$$F(R) = \frac{(1-R)^2}{2R}$$

Where F(R) is the reflectance coefficient (equivalent to absorption coefficient α) and R is the reflectance. The band gap are estimated by plotting $[F(R).h\upsilon]^2$ vs energy (eV) and extrapolation of linear region of the Tauc curve (figure 4.15).
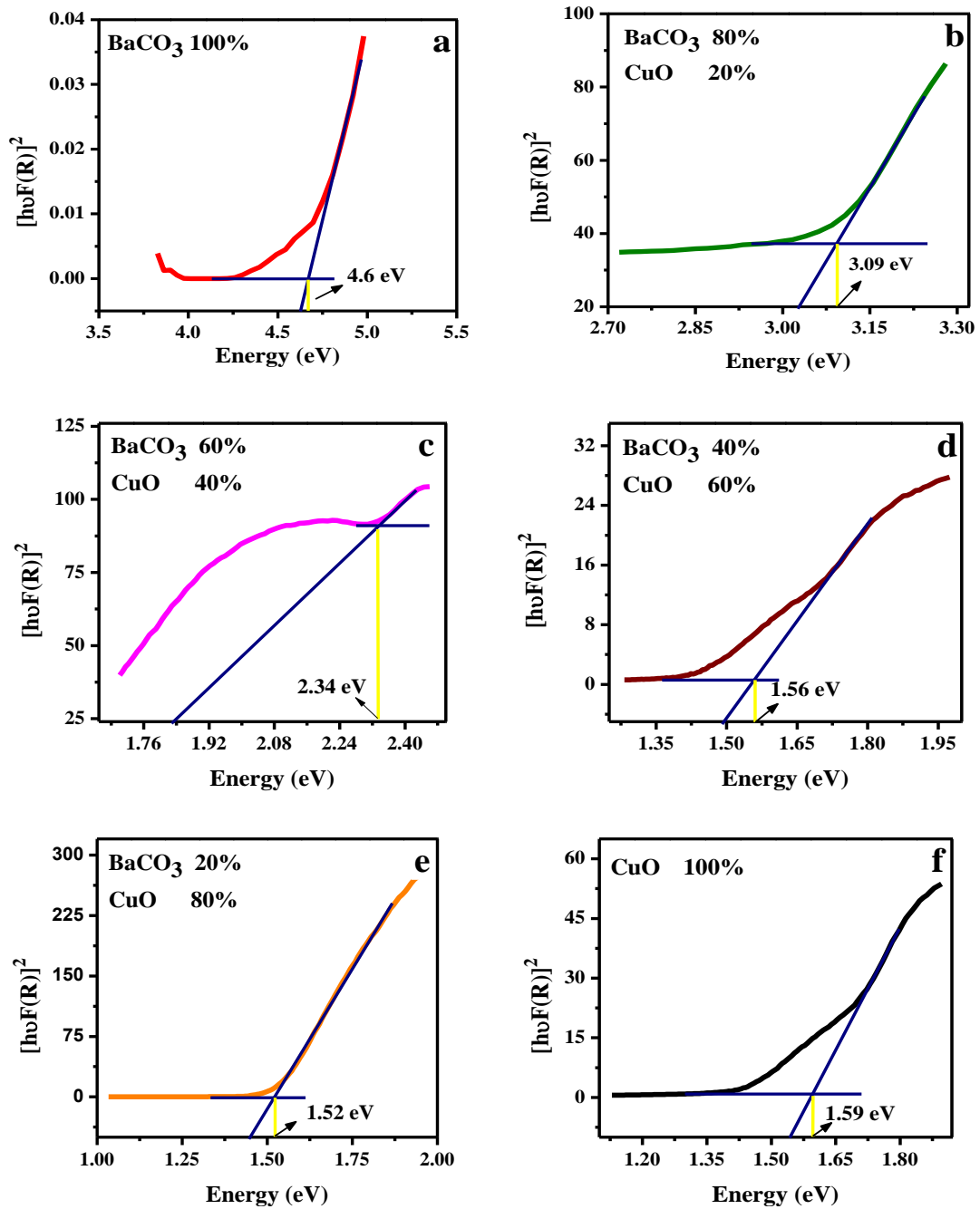
Figure 4.15: Optical band gap of samples: (a) BaCO₃, (b)-(c) Composites (BaCO₃; 80%, 60%, 40%, 20%), (f) CuO.

It can be seen from the graphs that on increasing CuO concentration in the samples the bandgap of the composites decreases trending towards the semiconductor behavior (Table 4.3). Composite C and D show lowest band gap due to pronounced amorphous effect which is induced by the structural disorders [88].

Table 4.3: Optical band gaps of different composites.

Samples	Band gap Energy Values (E_g) (eV)
$BaCO_3$	4.60
A	3.09
B	2.33
C	1.56
D	1.52
CuO	1.59

4.5.2. Dielectric Properties

Dielectric is the property of a material that transmits the electric force without allowing the electric charges to flow through the material rather they only shift from their equilibrium positions resulting into dielectric polarization which arranges the charges according to the external applied field. If the material has weakly bonded molecules, they will become polarized and will also reorient themselves according to field. By studying the dielectric properties, one can determine the application of materials in energy storage devices, supercapacitors, microwave applications, optics and solid state physics. There are multicomponent polarizations, operating at different frequencies, which contribute to the overall dielectric ability of a material [89].

- Electronic polarization.
- Ionic polarization.
- Dipolar polarization
- Interfacial polarization

Here we will focus on interfacial polarization which operates at room temperature and lower frequency (100 Hz to 5 MHz) as compared to the other types.

The dielectric measurements were carried out and the following quantities were calculated to study the device applications of the prepared samples.

- Dielectric constant
- Dielectric loss
- Tangent loss
- AC Conductivity

The dielectric parameter is represented as $\varepsilon^* = \varepsilon' - i\varepsilon''$ in which ε' is the real part of dielectric constant and $i\varepsilon''$ is the imaginary part. The real part explains the two fundamental characteristics of a material; the conductive nature which is the ability to transfer the electronic charge and the second is the capacitive nature which represents the energy storing ability of a material. It is calculated by the following expression [90]:

$$\varepsilon' = \frac{C \times d}{A \times \varepsilon_o}$$

Where C is the Capacitance, d is the sample thickness (m), A is the surface area of the sample (m^2), and ε_o is the permittivity of free space (8.854×10^{-12} F/m)

Dielectric loss (ε'') is the imaginary part which represents the energy dissipated during polarization while the real part is called the tangent loss (tanδ) which gives the quantitative energy loss. Dielectric and tangent loss can be expressed as [90]:

$$\varepsilon'' = \varepsilon' \times Dissipation\ factor$$

$$tan\delta = \frac{\varepsilon''}{\varepsilon'}$$

AC Conductivity (σ_{AC}) is the ability of a material to allow the passage of alternating current through it. It is given by [91]:

$$\sigma_{ac} = 2\pi f \varepsilon' \varepsilon_o tan\delta$$

The prepared samples were pressed into 10 mm pellets via cold press. The pellets were then placed one by one in between the electrodes and the measurements were made.

Figure 4.16 indicates the frequency dependent behavior of dielectric constant of the prepared samples, decreasing trend with increasing frequency. A dielectric medium is presumed to be composed of well conducting grains that are separated by resistive or poorly conductive grain boundaries. When the external field is applied, the charge carriers tend to align themselves according to the applied field and end up accumulating at the grain boundaries resulting in large polarization leading to high dielectric constant at low frequency as grain boundaries are more effective as compared to grains in electrical conduction. Interfacial polarization also contributes towards high dielectric constant due to the presence of inhomogeneities (porosity, defects and grain structure) in the structure [90], [92]. Crystallite size also affects the dielectric properties, since $BaCO_3$ may introduce poorly conducting grain boundary and CuO may introduce comparatively highly conducting grains. Thus reduction in size can produce more grain boundaries thereby increasing the changes in electric polarization at the grain boundaries. The Composites A-C show regular trend but D shows higher dielectric constant due to combined effect of above mentioned factors. As the frequency increases, the dipoles, created previously, lag behind in arranging themselves with the rapidly fluctuating alternating electric field thereby resulting in decreased dielectric constant value. On further increasing the frequency, the external field no longer affects the dielectric behavior and it becomes constant. CuO shows dielectric constant of 1.6×10^4 while $BaCO_3$ shows high dielectric constant 4.2×10^4, on increasing CuO concentration the dielectric constant of the composites decreases.
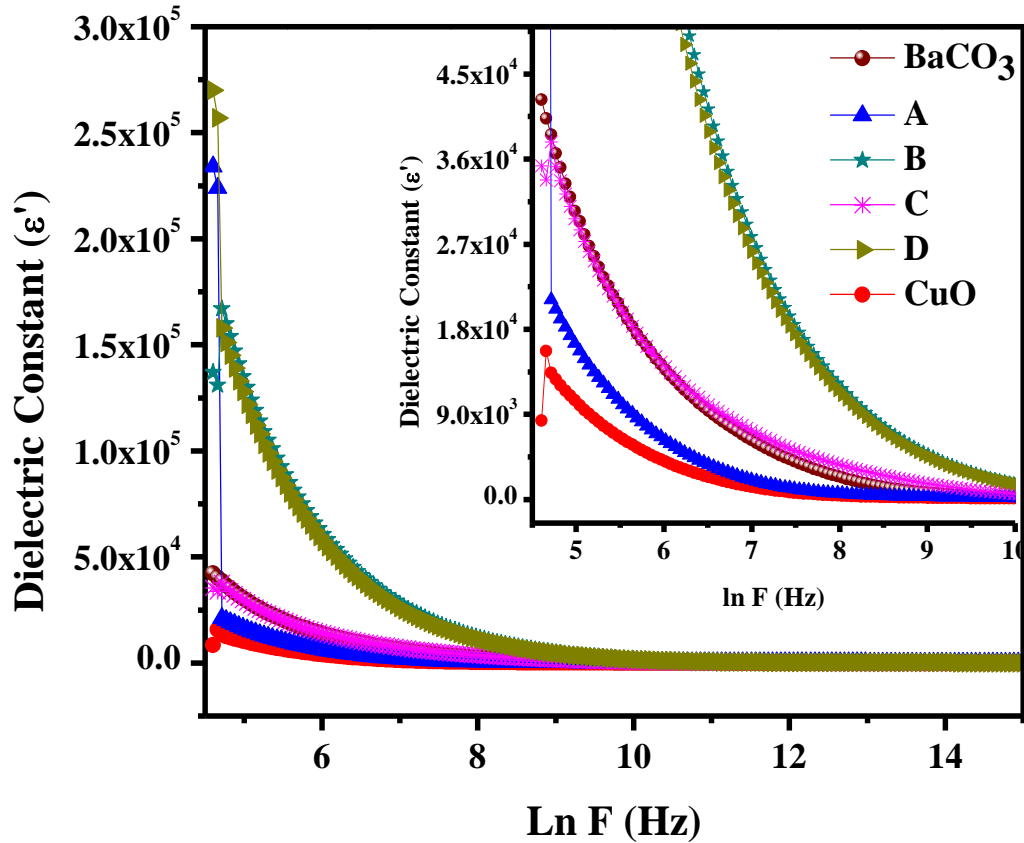
Figure 4.16: Dielectric constant of prepared samples at room temperature.

Similar behavior was observed for dielectric loss (figure 4.17), as the concentration of $BaCO_3$ increases, more energy is required to transfer electrons from one atom to another which results in high dielectric loss value and another reason is the heat generation due to rapid alignment of dipoles with the fluctuating electric field. At the higher frequency, less energy is consumed for hopping of electrons thereby decreasing the conduction leading to small energy loss.
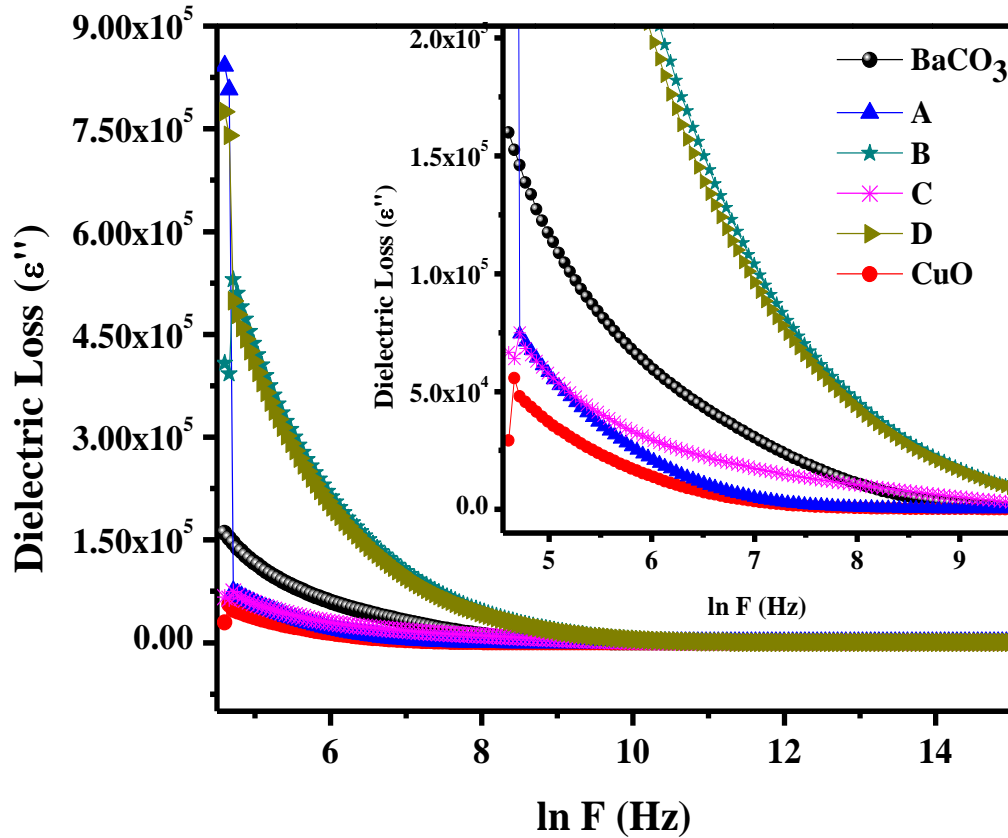
Figure 4.17: Dielectric loss of prepared samples at room temperature.

The tangent loss (tanδ) gives the relative energy loss. It can be seen from figure 4.18 that at low frequency the tan δ shows resonance peak with increased amplitude which arises when the frequency of the electron hopping within the sample resonates with the frequency of the applied external field. Pure $BaCO_3$ shows the maximum value of tanδ as compared to other samples. Comparatively tanδ exhibits smaller values and no systematic trend is observed which requires more study to have a clear understanding as well as temperature dependence on tanδ can be measured for better explanation of the obtained trend.
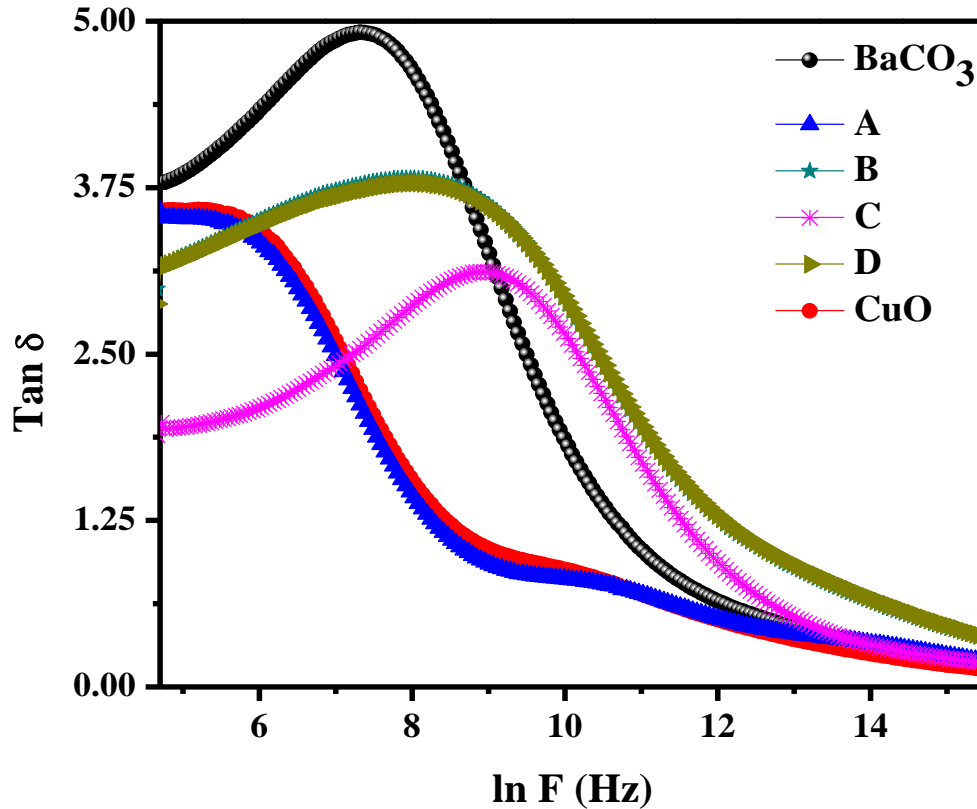
Figure 4.18: Tan loss of prepared samples at room temperature.

4.5.3. AC Conductivity

The variation of AC conductivity with frequency is shown in figure 4.19. To understand the behavior the graph is divided into three regions; a: low frequency region, b: mid frequency region and c: high frequency region. In low frequency region resonance between frequencies of electron hopping and external field occurs due to which a peak with high amplitude is shown while in CuO and composite A, no resonance occurs because charge carriers easily align themselves according to applied field. In the mid frequency region two relaxation phenomena occur, either a successful hopping in which

the electrons after hopping remain on their new site (translational) or they jump back to initial state causing unsuccessful hopping (reorientational). These mechanisms compete with each other and their ratios determine this dispersive region In high frequency region, due to rapid fluctuation in the external field the charge carriers do not get enough time to transfer to the new lattice site (atom) so they vibrate about the mean position causing the AC Conductivity to decrease initially but as the frequency continues to increase, AC Conductivity also increases indicating the domination of hopping conduction over band conduction [93]–[95].

Figure 4.19: AC Conductivity of prepared samples at room temperature.

Dielectric measurements along with AC Conductivity values have been shown in table 4.4.

Table 4.4: Dielectric Constant (ε'), Dielectric Loss (ε''), Tangent Loss (tanδ) and AC Conductivity (σ_{AC}) as a function of frequency at room temperature.

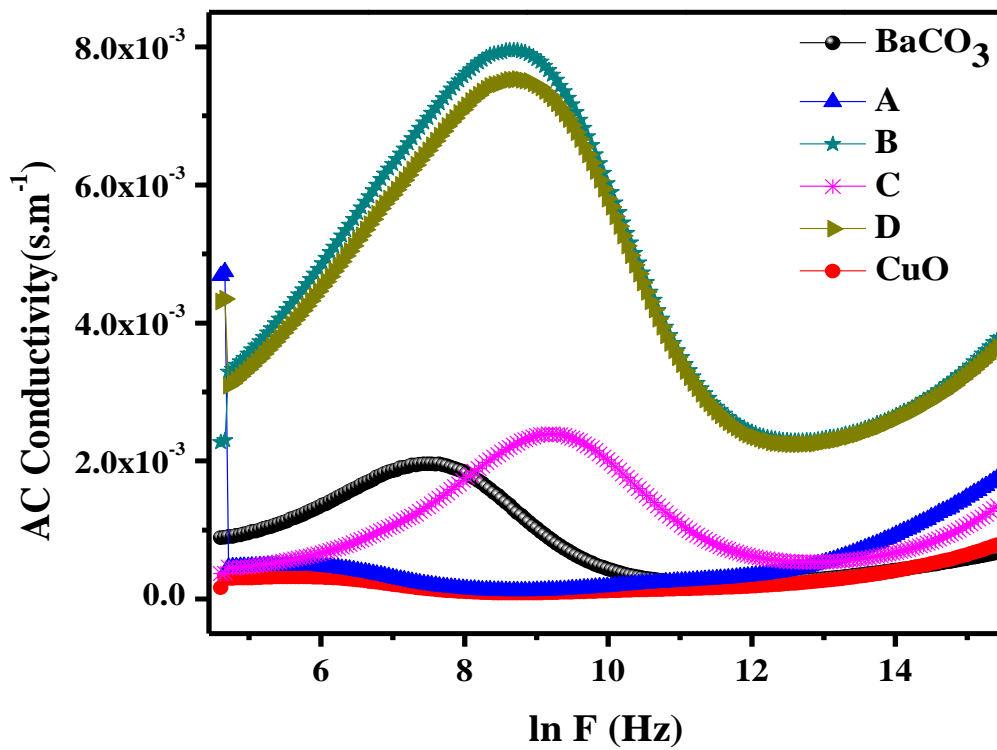| Samples	BaCO$_3$	A	B	C	D	CuO
ε' **(100 Hz)**	4.23×10^4	2.34×10^5	1.37×10^5	3.53×10^4	2.70×10^5	8.34×10^3
ε' **(5 MHz)**	16.9	32.4	36.7	26.0	33.9	20.6
ε'' **(100 Hz)**	1.60×10^5	8.42×10^5	4.08×10^5	6.66×10^4	7.75×10^5	2.93×10^4
ε'' **(5 MHz)**	2.41	6.33	13.6	4.86	13.1	2.84
tanδ **(100 Hz)**	3.78	3.59	3.00	1.89	2.87	3.52
tanδ **(5 MHz)**	0.14	0.19	0.37	0.18	0.38	0.13
σ_{AC} **(100 Hz) (s/m)**	8.88×10^{-4}	4.68×10^{-3}	2.27×10^{-3}	3.70×10^{-4}	4.31×10^{-3}	1.63×10^{-4}
σ_{AC} **(5 MHz) (s/m)**	6.71×10^{-4}	1.76×10^{-3}	3.78×10^{-3}	1.35×10^{-3}	3.65×10^{-3}	7.88×10^{-4}

4.6.   Conclusions and Future Prospects

BaCO$_3$ and CuO have been successfully synthesized via precipitation method. Atmospheric CO$_2$ furnished the carbon for carbonate synthesis. XRPD has confirmed the phases, purity and crystallite size while morphological analysis indicated the spherical geometry of the prepared samples by FESEM. The composites of BaCO$_3$/CuO were synthesized via palletization of the solid ground powders in four different compositions. FTIR was employed to analyze the vibrational bands of composites. A band in the range 1410-1450 cm^{-1} confirmed the presence of CO$_3^{2-}$ in the samples while TGA was used to determine the thermal behavior of BaCO$_3$ to confirm the CO$_2$ chemisorption. BaCO$_3$ underwent cyclic heat treatment and it was depicted that the CO$_2$ absorbance reduces sharply at first but remains the same after 3 cycles. The effect of CuO on sorption and desorption of BaCO$_3$ showed the formation of BaCuO$_2$, also confirmed by XRPD, which catalyzes desorption but arrests the sorption of CO$_2$. Optical band gap is found to decrease from 3.09 eV to 1.52 eV as CuO concentration increases in the composites.

Whereas, composites show high dielectric values (10^4 to 10^5) at low frequency (100 Hz) which makes them suitable for supercapacitor applications. However, composites showed higher dielectric loss values as compared to pure sample making them excellent candidate for microwave absorption applications. Alternating current (AC) conductivity showed unique variation with frequency which can be explained by translational and reorientational hopping.

The study of dielectric properties as a function of temperature can be carried out for further reasoning of the obtained trends. The crystallite size of the samples can be reduced further to understand its effects on the properties more clearly.

References

[1]   D. Hull and T. W. Clyne, *An introduction to composite materials*. Cambridge University Press, 1996.

[2]   M. Kutz, *Handbook of materials selection*. Wiley, 2002.

[3]   M. Balasubramanian, *Composite materials and processing*. CRC Press, 2013.

[4]   K. K. Chawla, *Composite materials: science and engineering*. Springer, 1998.

[5]   G. Akovali, *Handbook of composite fabrication*. Rapra Technology, 2001.

[6]   C. Suryanarayana and M. G. Norton, *X-ray diffraction: A practical approach*. Springer US, 2013.

[7]   R. Das, E. Ali, S. Bee, and A. Hamid, "Current applications of X-ray powder diffraction-a review," *Rev.V Adv. Mater. Sci.*, **38**, pp. 95–109, 2014.

[8]   S. Charurvedi and P. N. Dave, "Microscopy in nanotechnology," *Curr. Microsc. Contrib. to Adv. Sci. Technol. (A. Méndez-Vilas, Ed.)*, pp. 14–16, 2012.

[9]   A. J. Nozik, G. Conibeer, and M. C. Beard, *Advanced concepts in photovoltaics*: Royal Society of Chemistry, 2014.

[10]   P. R. Griffiths, J. A. De Haseth, and J. D. Winefordner, *Fourier transform infrared spectrometry*, 2nd ed. Wiley, 2007.

[11]   J. Torrent and V. Barrón, "Diffuse reflectance spectroscopy," *Methods Soil Anal. Part 5. Mineral. Methods.*, pp. 367–385, 2008.

[12]   R. Lopez and R. Go, "Band-gap energy estimation from diffuse reflectance measurements on sol–gel and commercial TiO_2 : a comparative study," *J Sol-Gel Sci Technol*, **61**, pp. 1–7, 2012.

[13]   V. U. Bakshi and U. A. Bakshi, *Electronic measurements*. Technical Publications, 2007.

[14]   P. G. Wolynes and V. Lubchenko, *Structural glasses and supercooled liquids: theory, experiment, and applications*. Wiley, 2012.

[15]   J. Russell and R. Cohn, *Thermogravimetric analysis*. Book on Demand, 2012.

[16]   H. Song, K. Shah, E. Doroodchi, T. Wall, and B. Moghtaderi, "Analysis on chemcial reaction kinetics of CuO/SiO_2 oxygen carriers for chemical looping air separation," *Energy & fuels*, **28**, pp. 173–182, 2014.

[17]   R. Pal, *Electromagnetic, mechanical, and transport properties of composite materials*. Taylor & Francis, 2014.

[18]   S. Thomas, K. Joseph, S. K. Malhotra, K. Goda, and M. S. Sreekala, *Polymer*

composites, macro- and microcomposites. Wiley, 2012.

[19] A. S. Bambal, *Mechanical evaluation and FE modeling of composite sandwich panels*. West Virginia University Libraries, 2007.

[20] J. P. Singh, *Processing, properties, and design of advanced ceramics and composites: ceramic transactions*. Wiley, 2016.

[21] X. Huang and P. Jiang, "Core-shell structured high-k polymer nanocomposites for energy storage and dielectric applications," *Adv. Mater.*, **27**, pp. 546–554, 2015.

[22] P. Barber *et al.*, "Polymer composite and nanocomposite dielectric materials for pulse power energy storage," *Materials (Basel).*, **2**, pp. 1697–1733, 2009.

[23] A. Pantano, *Carbon nanotube based composites: processing, properties, modelling and application*. Smithers Information Limited, 2012.

[24] A. Sajnani, M. N. Hedge, and C. Shetty, "Optical properties of composites.," *Int. J. Pharm. Ther.*, **5**, pp. 9–13, 2014.

[25] T. An, B. Pant, S. Yun, M. Park, S. Park, and H. Kim, "Mechanical and optical properties of electrospun nylon-6,6 nano fiber reinforced cyclic butylene terephthalate composites," *J. Ind. Eng. Chem.*, pp. 1–5, 2017.

[26] A. P. Mouritz and A. G. Gibson, *Fire properties of polymer composite materials*. Springer Netherlands, 2007.

[27] G. Gupta, A. Kumar, R. Tyagi, and S. Kumar, "Application and future of composite materials : a review," *Int. J. Innov. Res. Sci. Eng. Technol.*, **5**, pp. 6907–6911, 2016.

[28] M. E. Hossain, "The current and future trends of composite materials: an experimental study," *J. Compos. Mater.*, **45**, pp. 2133–2144, 2011.

[29] N. Tipcompor, T. Thongtem, A. Phuruangrat, and S. Thongtem, "Characterization of $SrCO_3$ and $BaCO_3$ nanoparticles synthesized by cyclic microwave radiation," *Mater. Lett.*, **87**, pp. 153–156, 2012.

[30] P. Patnaik and D. Ph, *Handbook of inorganic chemicals*. McGraw-Hill, 2003.

[31] W. Withering and R. Kirwan, "Experiments and observations on the Terra Ponderosa, &c. By William Withering, M. D.; Communicated by Richard Kirwan, Esq. F. R. S.," *Phil. Trans. R. Soc. L.*, **74**, pp. 293–311, 1784.

[32] I. Arvanitidis, D. Siche, and S. Seetharaman, "A study of the thermal decomposition of $BaCO_3$," *Metall. Mater. Trans. B*, **27**, pp. 409–416, 1996.

[33] R. Strobel, M. Maciejewski, S. E. Pratsinis, and A. Baiker, "Unprecedented formation of metastable monoclinic $BaCO_3$ nanoparticles," *Thermochim. Acta*, **445**, pp. 23–26, 2006.

[34] M. A. Alavi and A. Morsali, "Alkaline-earth metal carbonate, hydroxide and oxide nano-crystals synthesis methods , size and morphologies consideration," in *Nanocrystal*, Dr. Yoshitake Masuda, Ed. InTech, 2011.

[35] T. Thongtem, N. Tipcompor, A. Phuruangrat, and S. Thongtem, "Characterization of SrCO$_3$ and BaCO$_3$ nanoparticles synthesized by sonochemical method," *Mater. Lett.*, **64**, pp. 510–512, 2010.

[36] A. Zelati, A. Amirabadizadeh, and A. Kompany, "Preparation and characterization of barium carbonate nanoparticles," *Int. J. Chem. Eng. Appl.*, **2**, pp. 299–303, 2011.

[37] M. Ma, Y. Zhu, G. Cheng, and Y. Huang, "Fabrication and characterization of BaCO$_3$ nanostructures," *Mater. Lett.*, **62**, pp. 3110–3113, 2008.

[38] J. Xu and D. Xue, "Chemical synthesis of BaCO$_3$ with a hexagonal pencil-like morphology," *J. Phys. Chem. Solids*, **67**, pp. 1427–1431, 2006.

[39] C. Karagiozov and D. Momchilova, "Synthesis of nano-sized particles from metal carbonates by the method of reversed mycelles," *Chem. Eng. Process.*, **44**, pp. 115–119, 2005.

[40] Y. Ni, H. Zhang, J. Hong, L. Zhang, and X. Wei, "PAM-directed fabrication , shape evolution and formation mechanism of BaCO$_3$ crystals with higher-order superstructures," *J. Cryst. Growth*, **310**, pp. 4460–4467, 2008.

[41] Q. Zhang, C. Chen, and L. Fang, "Synthesis of thorny BaCO$_3$ dendritic structures via a simple PEG-assisted method," *Mater. Chem. Phys.*, **111**, pp. 191–194, 2008.

[42] S. Lv, J. Sheng, S. Zhang, and W. Sun, "Effects of reaction time and citric acid contents on the morphologies of BaCO$_3$ via PVP-assisted method," *Mater. Res. Bull.*, **43**, pp. 1099–1105, 2008.

[43] A. Omrani, A. A. Rostami, and E. Sedaghat, "Kinetics of cure for a coating system including DGEBA (n = 0)/1,8-NDA and barium carbonate," *Thermochim. Acta*, **497**, pp. 21–26, 2010.

[44] T. Hong, F. Chen, and C. Xia, "Barium carbonate nanoparticle to enhance oxygen reduction activity of strontium doped lanthanum ferrite for solid oxide fuel cell," *J. Power Sources*, **278**, pp. 741–750, 2015.

[45] P. C. Nagajyothi, M. Pandurangan, T. V. M. Sreekanth, and J. Shim, "In vitro anticancer potential of BaCO$_3$ nanoparticles synthesized via green route," *J. Photochem. Photobiol. B Biol.*, **156**, pp. 29–34, 2016.

[46] P. Hlabela, J. Maree, and D. Bruinsma, "Barium carbonate process for sulphate and metal removal from mine water," *Mine Water Environ.*, **26**, pp. 14–22, 2007.

[47] H. Zhang, C. Hu, M. Zhang, R. Yang, and C. Zheng, "Synthesis of $BaCO_3$ nanowires and their humidity sensitive property," *J. Nanosci. Nanotechnol.*, **11**, pp. 10706–10709, 2011.

[48] X. Wu, L. Wang, F. Luo, B. Ma, C. Zhan, and Y. Qiu, "$BaCO_3$ modification of TiO_2 electrodes in quasi-solid-state dye-sensitized solar cells : performance improvement and possible mechanism," *J. Phys. Chem. C*, **111**, pp. 8075–8079, 2007.

[49] E. Brzozowski, J. Sanchez, and M. S. Castro, "$BaCO_3$–TiO_2 solid state reaction : a kinetic study," *J. Mater. Synth. Process.*, **10**, pp. 2–6, 2002.

[50] S. P. More and R. J. Topare, "The review of various synthesis methods of barium titanate with the enhanced dielectric properties," in *International Conference on Condensed Matter and Applied Physics*, AIP Conference Proceedings **1728**, pp. 020560-1–020560-6, 2016

[51] V. P. Pavlovic, B. D. Stojanovic, V. B. Pavlovic, Z. Marinkovic-Stanojevic, Lj. Živković, and M. M. Ristic, "Synthesis of $BaTiO_3$ from a mechanically activated $BaCO_3$-TiO_2," *Sci. Sinter.*, **40**, pp. 21–26, 2008.

[52] H. H. Singh, A. D. Sharma, and H. B. Sharma, "Dielectric and electrical properties of Barium Zirconate Titanate ceramics," in *2 Days National Conference on Innovations in Science and Technology (NCIST-17)*, 2017.

[53] K. E. Oksuz, S. Sen, and U. Sen, "Influence of ZrO_2 addition on the structure and dielectric properties of $BaTiO_3$ ceramics," *Acta Phys. Pol. A*, **131**, pp. 197–199, 2017.

[54] H. Zehra, Z. Aydin, O. Yilmaz, and S. Turgut, "Ultrasonics sonochemistry effects of ultrasonication and conventional mechanical homogenization processes on the structures and dielectric properties of $BaTiO_3$ ceramics," *Ultrason. Sonochem.*, **34**, pp. 873–880, 2017.

[55] M. K. El-Mansy, N. M. Shash, M. H. Maklad, and E. M. Diefallah, "Effect of growing barium ferrite phases on the electrical conduction in Fe_2O_3/$BaCO_3$ composite," *Mater. Chem. Phys.*, **52**, pp. 71–77, 1998.

[56] S. Capraro *et al.*, "Barium ferrite thick films for microwave applications," *J. Magn. Magn. Mater.*, **272–276**, pp. E1805–E1806, 2004.

[57] W. Widanarto, M. Jandra, S. K. Ghoshal, M. Effendi, and W. T. Cahyanto, "$BaCO_3$ mediated modifications in structural and magnetic properties of natural nanoferrites," *J. Phys. Chem. Solids*, **79**, pp. 78–81, 2015.

[58] Q. He, H. Z. Wang, G. H. Wen, Y. Sun, and B. Yao, "Formation and properties of

$Ba_xFe_{3-x}O_4$ with spinel structure by mechanochemical reaction of α-Fe_2O_3 and $BaCO_3$," *J. Alloys Compd.*, **486**, pp. 246–249, 2009.

[59] F. Zhang, X. Wang, X. Zhang, M. Tursun, and H. Yu, "Promotion by Co of a NiO-$BaCO_3$ catalyst for N_2O decomposition," *Chinese J. Catal.*, **36**, pp. 344–347, 2015.

[60] A. K. Zak, A. M. Hashim, and M. Darroudi, "Optical properties of $ZnO/BaCO_3$ nanocomposites in UV and visible regions.," *Nanoscale Res. Lett.*, **9**, p. 399, 2014.

[61] V. A. Gasparov *et al.*, "Superconducting and anomalous electron transport properties and electronic structure," *Phys. Rev. B*, **63**, pp. 1–9, 2001.

[62] G. K. Strukova *et al.*, "On the synthesis and the electric and magnetic properties of superconducting barium–niobium–oxide compounds," *Phys. C*, **291**, pp. 207–212, 1997.

[63] G. Chen and B. Qi, "Barium niobate formation from mechanically activated $BaCO_3$-Nb_2O_5 mixtures," *J. Alloys Compd.*, **425**, pp. 395–398, 2006.

[64] C. Sun *et al.*, "$BaNbO(IO_3)_5$: A new polar material with a very large SHG response," *J. Am. Chem. Soc*, **131**, pp. 9486–9487, 2009.

[65] M. Zhang, C. Hu, H. Liu, Y. Xiong, and Z. Zhang, "A rapid-response humidity sensor based on $BaNbO_3$ nanocrystals," *Sensors Actuators B*, **136**, pp. 128–132, 2009.

[66] E. J. Wildman, A. C. Mclaughlin, J. F. Macdonald, J. V Hanna, and J. M. S. Skakle, "The crystal structure of $Ba_3Nb_2O_8$ revisited: A neutron diffraction and solid-state NMR study," *Inorg. Chem.*, **58**, pp. 2–10, 2017.

[67] K. Yuan *et al.*, "Formation of barium zirconate fibers for high-temperature thermal insulation applications," *J. Am. Ceram. Soc*, **99**, pp. 2913–2919, 2016.

[68] M. Ahrens and J. Maier, "Thermodynamic properties of $BaCeO_3$ and $BaZrO_3$ at low temperatures," *Thermochim. Acta*, **443**, pp. 189–196, 2006.

[69] S. Yamanaka *et al.*, "Thermophysical properties of BaZrO3 and BaCeO3," *J. Alloys Compd.*, **359**, pp. 109–113, 2003.

[70] D. Medvedev, A. Murashkina, E. Pikalova, A. Demin, and A. Podias, "Progress in materials science $BaCeO_3$: materials development , properties and application," *Prog. Mater. Sci.*, **60**, pp. 72–129, 2014.

[71] S. Matsubara, S. Kaneko, S. Morimoto, and S. Shimizu, "A practical capacitive type CO_2 sensor using $CeO_2/BaCO_3/CuO$ ceramics," *Sensors Actuators B*, **65**, pp. 128–132, 2000.

[72] T. Itoh, "Role of CuO for the decarbonation of $BaCO_3$ and $CaCO_3$ in the solid-state reaction of CuO with $BaCO_3$ and that of CuO with $CaCO_3$," *J. Mater. Sci. Lett.*, **22**, pp. 185–189, 2003.

[73] S. W. Sofie and F. Dogan, "Effect of carbon on the microstructure and superconducting properties of $YBa_2Cu_3O_{7-x}$ melt-textured crystals," *Supercond. Sci. Technol.*, **15**, pp. 735–740, 2002.

[74] A. S. Haja Hameed, C. Karthikeyan, V. Senthil Kumar, S. Kumaresanb, and G. Ravic, "Impact of alkaline metal ions Mg^{2+}, Ca^{2+}, Sr^{2+} and Ba^{2+} on the structural, optical, thermal and antibacterial properties of ZnO nanoparticles prepared by the co-precipitation method," *J. Mater. Chem. B*, **1**, pp. 1–45, 2013.

[75] M. Asgari, A. Ataie, and H. Sabarou, "Synthesis of $BaCO_3$ nano-particles through a polymer-assisted precipitation method," *J. Mater. Eng. Perform.*, **23**, pp. 826–832, 2014.

[76] C. Zhu and M. J. Panzer, "Seed layer-assisted chemical bath deposition of CuO films on ITO-coated glass substrates with tunable crystallinity and morphology," *Chem. Mater.*, **26**, pp. 2960–2966, 2014.

[77] H. Siddiqui, M. S. Qureshi, and F. Z. Haque, "Optik Surfactant assisted wet chemical synthesis of copper oxide (CuO) nanostructures and their spectroscopic analysis," *Opt.-Int. J. Light Electron Opt.*, **127**, pp. 2740–2747, 2016.

[78] B. D. Cullity, *Elements of X-ray difrraction*. Addison-Wesley Publishing Company Inc, 1956.

[79] A. W. Burton, K. Ong, T. Rea, and I. Y. Chan, "On the estimation of average crystallite size of zeolites from the Scherrer equation : A critical evaluation of its application to zeolites with one-dimensional pore systems," *Microporous Mesoporous Mater.*, **117**, pp. 75–90, 2009.

[80] N. S. Gonçalves, J. A. Carvalho, Z. M. Lima, and J. M. Sasaki, "Size–strain study of NiO nanoparticles by X-ray powder diffraction line broadening," *Mater. Lett.*, **72**, pp. 36–38, 2015.

[81] P. M. Diehm, P. Agoston, and K. Albe, "Size-dependent lattice expansion in nanoparticles : reality or anomaly?," *ChemPhysChem*, **13**, pp. 2443–2454, 2012.

[82] S. S. Alias and A. A. Mohamad, *Synthesis of Zinc Oxide by sol-gel method for photoelectrochemical cells*. Springer Singapore, 2013.

[83] S. C. Shen, X. Chen, S. Kawi, S. C. Shen, X. Chen, and S. Kawi, "CO_2 adsorption over Si-MCM-41 materials having basic sites created by postmodification with La_2O_3," *Langmuir*, **20**, pp. 9130–9137, 2004.

[84] R. Philippt and K. Fujimoto, "FTIR spectroscopic study of CO_2 adsorption/desorption on MgO/CaO catalysts," *J. Phys. Chem.*, **96**, pp. 9035–9038, 1992.

[85] S. M. Tavender, S. A. Johnson, D. Balsom, A. W. Parker, and R. H. Bisby, "The carbonate, CO_3, in solution studied by resonance raman spectroscopy," *Laser Chem.*, **19**, pp. 311–316, 1999.

[86] F. A. Andersen and L. Brecevic, "Infrared spectra of amorphous and crystalline calcium carbonate," *Acta Chem. Scand.*, **41**, pp. 1018–1024, 1991.

[87] H. Lu, A. Khan, S. E. Pratsinis, and P. G. Smirniotis, "Flame-made durable doped-CaO nanosorbents for CO_2 capture," *Energy & fuels*, **23**, pp. 1093–1100, 2009.

[88] E. S. M. Goh, T. P. Chen, C. Q. Sun, and Y. C. Liu, "Thickness effect on the band gap and optical properties of germanium thin films," *J. Appl. Phys.*, **107**, pp. 2430-2-24305–5, 2010.

[89] H. M. El-Mallah, "AC electrical conductivity and dielectric properties of perovskite (Pb,Ca) TiO_3 ceramic," *Acta Phys. Pol. A*, **122**, pp. 174–179, 2012.

[90] I. H. Gul and A. Maqsood, "Structural, magnetic and electrical properties of cobalt ferrites prepared by the sol-gel route," *J. Alloys Compd.*, **465**, pp. 227–231, 2008.

[91] J. K. Rao, A. Raizada, D. Ganguly, M. M. Mankad, S. V. Satayanarayana, and G. M. Madhu, "Investigation of structural and electrical properties of novel CuO-PVA nanocomposite films," *J. Mater. Sci.*, **50**, pp. 7064–7074, 2015.

[92] A. Azam, A. S. Ahmed, M. S. Ansari, M. Shafeeq M, and A. H. Naqvi, "Study of electrical properties of nickel doped SnO_2 ceramic nanoparticles," *J. Alloys Compd.*, **506**, pp. 237–242, 2010.

[93] S. A. Soomro, I. H. Gul, M. Z. Khan, and H. Naseer, "Dielectric properties evaluation of $NiFe_2O_4$/MWCNTs nanohybrid for microwave applications prepared via novel one step synthesis," *Ceram. Int.*, **43**, pp. 4090–4095, 2017.

[94] K. Funke, "Jump relaxation in solid electrolytes," *Prog. Solid State Chem.*, **22**, pp. 111–195, 1993.

[95] N. Ortega, A. Kumar, P. Bhattacharya, S. B. Majumder, and R. S. Katiyar, "Impedance spectroscopy of multiferroic $PbZr_xTi_{1-x}O_3$/$CoFe_2O_4$ layered thin films," *Phys. Rev. B*, **77**, p. 14111, 2008.